# AMORPHIZATION AND DE-VITRIFICATION IN IMMISCIBLE COPPER-NIOBIUM ALLOY THIN FILMS

Anantharamakrishnan Puthucode Balakrishnan

Thesis Prepared for the Degree of

MASTER OF SCIENCE

UNIVERSITY OF NORTH TEXAS

May 2007

APPROVED:

Michael J. Kaufman, Major Professor and Chair of the Department of Materials Science and Engineering
Rajarshi Banerjee, Co-Advisor
Thomas Scharf, Committee Member
Nandika A D'Souza, Graduate Programs Coordinator
Oscar Garcia, Dean of the College of Engineering
Sandra L. Terrell, Dean of the Robert B. Toulouse School of Graduate Studies

Puthucode Balakrishnan, Anantharamakrishnan. Amorphization and De-vitrification in Immiscible Copper-Niobium Alloy Thin Films. Master of Science (Materials Science and Engineering), May 2007, 76 pp, 45 illustrations, references, 35 titles.

While amorphous phases have been reported in immiscible alloy systems, there is still some controversy regarding the reason for the stabilization of these unusual amorphous phases. Direct evidence of nanoscale phase separation within the amorphous phase forming in immiscible Cu-Nb alloy thin films using 3D atom probe tomography has been presented. This evidence clearly indicates that the nanoscale phase separation is responsible for the stabilization of the amorphous phase in such immiscible systems since it substantially reduces the free energy of the undercooled liquid (or amorphous) phase, below that of the competing supersaturated crystalline phases. The devitrification of the immiscible Cu-Nb thin film of composition Cu-45% Nb has been studied in detail with the discussion on the mechanism of phase transformation. The initial phase separation in the amorphous condition seems to play a vital role in the crystallization of the thin film. Detailed analysis has been done using X-ray diffraction, Transmission electron microscopy and 3D atom probe tomography.

ACKNOWLEDGMENTS

I would like to thank my advisor Prof. Michael J. Kaufman for all his help over the years, both academically and personally. I would like to specially thank him for the trust he had in me while taking me as a student although I came from a different background. His faith and confidence always kept me motivated. I am extremely thankful to him for being patient with me in learning things from the scratch upto the completion of this thesis. I am also very thankful to Dr. Rajarshi Banerjee for co-advising my thesis and spending his precious time explaining some of the concepts in thermodynamics. He has also been a very good friend to me and helped me out on a number of occasions. I would like to thank my committee member Dr. Thomas Scharf for his valuable suggestions and being a very nice and understanding person.

I would specially like to thank Dr. Nandika D'Souza, the graduate coordinator, who was very helpful in completing the admission and transfer procedures. I would also like to thank Alberta Caswell for being warm and friendly from the day I came to the department. I would like to thank my colleagues Junyeon Hwang and David Diercks for all their help and support over the past years. I would also like to thank Evan Stenmark (REU student) for his help in setting up the Advanced Metallic Materials Laboratory. I would like to acknowledge Vaishali for helping me conduct some heat-treatment experiments and Uma for helping me with her suggestions on writing the thesis.

Last, but not the least, I would like to thank my family for being very supportive and encouraging in every step. I really feel lucky to have such wonderful parents, an excellent university and the opportunity to work with some of the best characterization equipments at UNT.

TABLE OF CONTENTS

Page

LIST OF FIGURES

Page

# CHAPTER 1

# INTRODUCTION

The continuing interest in metallic thin films and multilayers is motivated by their structural, optical, magnetic and transport properties which are novel when compared with bulk materials. The transport properties are interesting since they are fundamental properties of a metal and have relevance for the commercially important phenomena of magnetoresistance and giant magnetoresistance (GMR) in magnetic recording media. Also, the development of interconnection materials with high electromigration resistance and low resistivity is essential to the manufacture of very large scale intergrated (VLSI) devices. In recent years, there is a high demand for materials with low electrical resistivity used as interconnects.[1] At high current densities (>106 A/cm$^2$), metallic aluminum and aluminum-based metallization are prone to electromigration damage leading to catastrophic circuit failure.[2]

Copper is currently being used in metallization due to its low resistivity, high electromigration and stress migration resistance. It has been reported that Cu with insoluble atoms can decrease the resistivity close to that of pure Cu.[3] Copper is known to be immiscible with insoluble elements such as C, Mo, Nb, W, Ta, etc. in both solid and liquid states. The equilibrium phase diagram (Fig. 1.1) of Cu-Nb shows that Cu and Nb are mutually insoluble with each other in solid and liquid states. Being a non-equilibrium process, film formation by sputter deposition may result in an enhancement of the solid solubility, dramatic changes in the defect density, the formation of metastable structures as well as changes in the microstructure of

alloy films. Cu and Nb do not form any compounds or alloys by conventional bulk processing techniques and hence the sputtering becomes a suitable choice to synthesize Cu-Nb films.

While amorphous phases have been reported in immiscible alloy systems, there is still some controversy regarding the reason for the stabilization of these unusual phases. For instance, there are several questions that need to be answered regarding the metastability of the amorphous phase in Cu-Nb thin films. Issues like nanoscale phase separation have been addressed in this study. 3D atom probe tomography (3DAP) is a unique technique for three dimensional atomic level characterizations that has been used to obtain direct evidence of nanoscale phase separation within the amorphous phase. Further heat treatments have been performed on the same Cu-Nb thin films to study the decomposition of amorphous Cu-Nb thin film. 3D Atom Probe Tomography results have been correlated with x-ray diffraction and transmission electron microscopy (TEM) results.

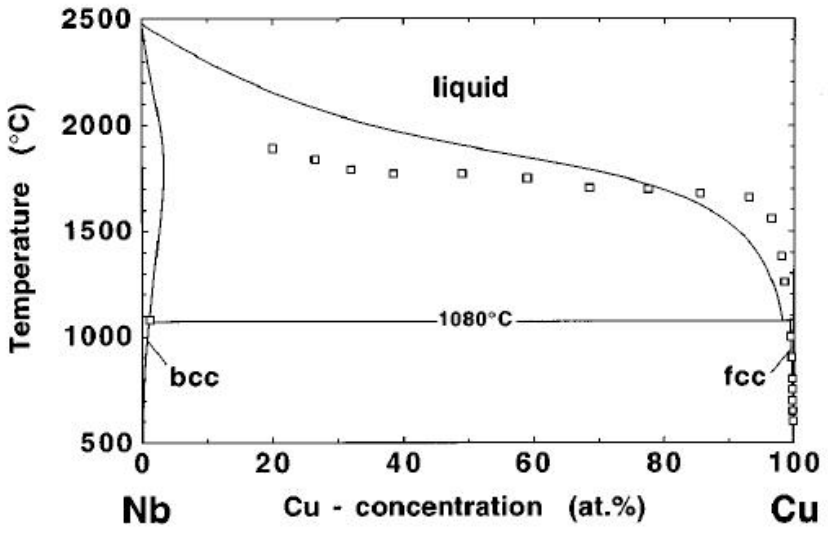


*Fig 1.1: Equilibrium phase diagram of Cu-Nb.*

# CHAPTER 2

# REVIEW OF LITERATURE

## 2.1 Introduction

The development of new alloys has been and continues to be one of the important aspects of materials science. The structure of alloys, the theory of alloying and the various properties offered by the mixing of elements have been topics of interest for a long time. The progress in technology and the availability of new characterization techniques coupled with computational modeling has accelerated growth in the area of materials science. The study of amorphous alloy has been one such area where a lot of interest has been shown since its inception in 1960 from the work done by Duwez et al. at Caltech.[4] The practical applications were not considered seriously in the beginning owing to the limited size and cost of the constituent elements in the alloys such as precious metals like, Au, Pd, and Pt. The first possible application of these alloys was an Fe-P-C alloy (synthesized in the form of thin ribbons) which had strong ferromagnetic property at room temperature.[5] Amorphous alloys in the form of thin films have also shown interesting magnetic and transport properties, which have applications in the semiconductor and magnetic data storage industries. The formation of amorphous alloys can be thermodynamically classified into two broad systems: negative $\Delta H_{mix}$ (heat of mixing) systems and positive $\Delta H_{mix}$ systems. Bulk glass formers fall under the former category and have been studied in detail for a while, whereas the formation of amorphous alloys in the latter system has not been studied in detail and a lot of questions remain unanswered, some of which are addressed in this thesis.

## 2.2 Formation of Amorphous Phases

### 2.2.1 Negative ΔH Systems

As mentioned above, multi-component bulk metallic glasses are systems that exhibit negative ΔH. The structure and properties of metallic glasses have attracted a lot of interest towards potential engineering applications. With the development of continuous casting processes for the manufacture of metallic glasses, a lot of academic and industrial research resulted.[6] Turnbull et al. showed similarity between the metallic glasses and non-metallic glasses such as silicates, polymers and ceramic glasses by showing that metallic glasses manifest glass transition similar to conventional glass-forming melts.[7,8] The earliest bulk metallic glasses formed were Pd based alloys by Chen,[9] following which Inoue, W.L. Johnson and some others have been successful in preparing bulk metallic of different compositions.[10] A list of alloys with their compositions and the year which they were developed has been mentioned in reference 11.[11]

#### 2.2.1.1 Thermal Stability and Glass-Forming Ability of Metallic Glasses

The glassy state in metallic glasses is not an equilibrium state of solids, rather a metastable state that can only be achieved if the growth of competing crystalline equilibrium phases is avoided or suppressed. The kinetics controlling the crystal nucleation rate in undercooled liquids is given by Turnbull in his classical nucleation theory.[12,13] He also shows that the reduced glass transition temperature $T_{rg} = T_g/T_m$ is a key parameter in determining if the melt of a given material can form a glass or not. With the assumption that the shear viscosity, η, follows a Vogel-Fulcher-Tammann relation given by:

$$\eta = \eta_o \exp \frac{DT_o}{T - T_o}$$

Where $T_o$ is the Vogel-Fulcher temperature and D is known as the fragility parameter related to the liquid property,[14] and the nucleation rate proportional to $1/\eta$, Turnbull showed that materials with $T_{rg} \geq 2/3$ should be good glass formers. Thus, Turnbull's analysis suggests that to find bulk-glass forming systems, one should look for high $T_{rg}$.

Johnson suggests an effective way of forming an amorphous alloy with the help of his "confusion principle."[15] According to him, a large number of chemically different components in an alloy system frustrate the tendency to form a crystalline structure and would be associated with high atomic level strains, arising from different atomic sizes.[16] Inoue et al. summarized the results of glass forming ability in multicomponent alloys and proposed three empirical rules:[11] (1) alloy system contains more than three elements (2) the atomic size differences between the different elements should be more than 12% and (3) the constituents should have negative heat of mixing. They suggest that alloys satisfying the above rules favor the formation of amorphous metals.

2.2.1.2 Thermodynamic Perspective

From a thermodynamic point of view, bulk amorphous alloys show a low driving force for crystallization in the supercooled liquid region, which results in low nucleation rates and improved glass forming ability. Thermal analysis helps in the determination of the Gibbs free-energy difference between the supercooled liquid and crystalline solid, $\Delta G_{l\text{-}s}$, which can be calculated by integrating the specific heat capacity $\Delta C_p^{l\text{-}s}(T)$ according the equation given by:

$$\Delta G_{l-s}(T) = \Delta H_f - \Delta S_f T_o - \int_T^{T_o} \Delta C_p l - s(T) dT + \int_T^{T_o} \frac{\Delta C_p l - s(T)}{T} dT , \quad (1)$$

Where $\Delta H_f$ and $\Delta S_f$ are the enthalpy and entropy of fusion, respectively at temperature $T_o$, the temperature at which the crystal and the liquid are in equilibrium. A low free energy

means a low enthalpy and large entropy. The large entropy can be associated with the multicomponent alloys because it is proportional to the number of microscopic states.[17]

It has been shown that an increase in specific heat for metallic glass forming alloys is larger than pure metals such as In, Bi and Sn.[18] According to Kauzmann, with increasing undercooling, the entropy of a liquid approaches that of a crystalline state as indicated by the increase in specific heat.[19, 20] An isentropic temperature for metallic glass was found to be 0.6 $T_m$, below which the entropy of undercooled liquid would become less than that of a crystalline phase. Fig. 2.1 shows the Gibbs free energy difference between the supercooled liquid and the crystalline mixture of different glass formers.[21] It can be seen that the glass formers with lower critical cooling rates have smaller $\Delta G$ compared to the glass formers with higher critical cooling rates. This means that bulk metallic glass formers already have some free volume and that they tend to form short range order close to melting temperatures. All these facts are consistent with the assumption that the bulk metallic glass formers have high viscosity and are dense liquids at melting temperatures and when undercooled as well as the fact that the crystalline phases show large configurational entropy of mixing.

As discussed above, good glass formers should have high $T_{rg}$, which means that they should have low melting temperatures. With reference to this point alloys with high glass forming ability (GFA) can be found among alloy compositions with deep eutectics, which form liquids that are stable at relatively low temperatures. Some good glass formers are systems like Cu-Zr, Zr-Be, Pd-Si, Ni-Nb, which also show deep eutectics. In the ternary[22] and quaternary[23] systems Cu-Ti-Zr and Cu-Ni-Ti-Zr exhibit deeper eutectics and better GFA. Another parameter used to predict the GFA is $\Delta T_x = T_x - T_g$, the difference between the onset of crystallization and glass transition temperature, although for some compositions there is some disparity between $T_{rg}$

and $\Delta T_x$. A better parameter taking into account $T_x$, $T_g$ and $T_l$, where $T_l$ is the liquidus temperature has been defined by Lu and Liu.[24] They proposed that the parameter $\gamma = T_x/(T_g + T_l)$ predicts the GFA better for metallic glasses.

2.2.1.3 Kinetics Perspective

Glass transition from the molten state to the glassy state cannot be explained just as a thermodynamic process. The glass transition temperature depends on the heating or cooling rates during measurements. Viscosity, as mentioned previously, has a significant influence in the GFA of an alloy composition. A number of methods have been used to measure the viscosity at different temperature ranges down to the largely undercooled liquid near $T_g$.[25,26,27]

The first viscosity measurement was made on Vit4 close to the glass transition temperature using parallel-plate rheometry.[28] All viscosity data can be well defined by the Vogel-Fulcher-Tammann (VFT) relation. The high temperature rheological properties were measured using Couette viscosimeter. The data from the graph is used to characterize the glass-forming liquids as it reflects the change of mobility of atoms during undercooling.[27] $SiO_2$ is the strongest glass former with a fragility D of 100. The viscosity values of bulk metallic glasses (BMG) show that they are closer to the strong glass formers with D around 20. The melt viscosity is approximately three orders of magnitude more than pure metals. The relaxation behavior studied by neutron scattering on BMG forming liquids show that they are similar to strong liquids.[29,30] A strong liquid means higher viscosity and slower kinetics in the supercooled liquid region. This retards formation of stable nuclei and inhibits the growth of stable phases because of poor mobility of atoms.

Atomic diffusion is also an important parameter that affects the GFA of alloy systems. The first studies of atomic diffusion in the glassy state were conducted by Geyer et al.[31] They

found that the activation energy for diffusion in glass is much smaller than that of the supercooled liquid and attributed this to the transition of Be hopping in solid state to Be movement by a co-operative shear process in the liquid state. In another work by Masuhr et al.[32] they defined a time called characteristic jump time for atomic diffusion $\tau_D$ and compared it with the structural relaxation time $\tau = \eta/G_\infty$, where $G_\infty$ is the shear modulus. They found that the temperature dependence of Al self-diffusion compares with the temperature dependence of the equilibrium viscosity, whereas that of Be and Ni, which are smaller in size differ by three orders of magnitude at lower temperatures. They proposed that at lower temperatures smaller atoms do not act co-operatively whereas as temperature increases, the time for shear process becomes comparable to hopping times until eventually liquid like motion predominates at very high temperatures. Apparently it is material dependent and so is glass transition.

### 2.2.2 Positive ΔH Systems

In general the tendency for the formation of amorphous alloys has been largely seen in systems that exhibit negative heat of mixing (ΔH) for various reasons discussed in the previous section. However, there are many elements that do not form alloys at room temperature and pressure due the absence of a driving force. A brief survey of the binary phase diagrams[33] reveals some ‘‘immiscible systems,’’ in which the two constituent elements show little or no mutual solubility up to very high temperatures, even in the liquid state. Some of them include pair of simple elements such as Ag–Fe, Ag–Ni, Cu–W, and Ti–Mg. These systems are characterized by a large positive (ΔH) in both the liquid and solid states. There are other systems, e.g., Ag–Cu, Fe–Mg, and Fe–Cu, that have a positive ΔH but its magnitude is not as large such that the elements are miscible in the liquid state. This is due to the entropic contribution to the free energy of mixing at high temperatures. But at lower temperatures, such as room temperature, the

positive ΔH dominates, leading to phase separation, where the constituent elements become immiscible, exhibiting very small mutual solid solubility and no intermediate phases.

The syntheses of alloys between immiscible elements, and an understanding of the new phases, are clearly of considerable scientific and technologic interest. In addition to being a fundamental study of alloying theory and phase transformation, the alloys synthesized have also opened up new opportunities for tuning materials properties. For example, the effects of alloying on the magnetic properties of Fe (or Ni, Co, etc.) can be studied as a continuous function of the otherwise immiscible alloying element added.[34] The new alloy can also be the precursor for a granular mixture of immiscible elements from which giant magnetoresistance can be derived.[35] In ultra-thin films, the competition between phase separation (spinodal decomposition) and strain energy reduction enables the formation of self-assembled lateral multilayers of immiscible elements, as templates of modulated nanostructures.[36] Pattern formation through thermal decomposition of the alloy in the presence of external forcing actions (such as ion irradiation and plastic deformation) represents yet another possibility to take advantage of the non-equilibrium structures formed in immiscible systems.[37]

One of the key aspects that have often been left out from other discussions is the kind of "alloy" that has been, and can be created between immiscible elements using different processing techniques and under different processing conditions. The main idea of this thesis is to address such issues in detail. Some of the issues regarding the nature of the positive ΔH alloys created between immiscible elements that are listed below are intriguing as they pose challenges to our current understanding of alloys. To obtain a clear picture we need to understand the differences between the positive and negative ΔH systems with respect to characterization and processing conditions.

Systems with a negative ΔH assists spontaneous intermixing whereas in the positive ΔH systems the non-equilibrium alloys have to survive a thermodynamic driving force for phase decomposition. Hence, true atomic-level alloying and the chemical homogeneity of the constituent elements cannot be taken for granted, and difficult to prove. For most of the previous experiments, diffraction methods were the only techniques used to establish the formation, and characterize the structure, of the new alloys. In the case of crystalline alloys, recent models demonstrate that a decomposed microstructure, leads to a single set of diffraction peaks at the positions corresponding to the average lattice parameter of the two elements, close to that of a truly homogeneous supersaturated solution.[38] The broad diffraction peaks may also overlap if the crystal domain sizes are extremely small making it difficult to ascertain if a single-phase homogeneous alloy is formed.[8] Moreover, it is often difficult to distinguish between a mixture of nanocrystalline domains and a truly amorphous structure.[39]

Energy state reached by the alloys is another important factor to be discussed. Amorphous alloys with a negative ΔH have a free energy very close to that of equilibrium compounds, due to the substantial chemical and topological short-range order present in its structure. This is shown in Fig 2.2a. For easy glass formers the heat of crystallization is almost always less than a few kJ/mol. In the case of immiscible systems, which contain no low-energy equilibrium alloys and are marginal glass formers at best, it is difficult to predict a priori even the magnitude of the positive enthalpy of formation of the amorphous alloy, if it does get to form. Fig 2.2b gives a comparison of the enthalpy of formation in the immiscible systems.

## 2.3 Crystallization in Amorphous Alloys

There are several modes in crystallization of amorphous alloys. Fig. 2.3a illustrates a schematic free energy–composition curve for a hypothetical eutectic type alloy system which forms an amorphous phase by rapid solidification. The driving force for the crystallization from a rapidly-solidified amorphous phase can be graphically represented by the difference in free energy of the liquid phase (amorphous) and solid phase. The amorphous alloy with composition a or f can change the structure from amorphous to crystalline by reduction in its free energy without any change in composition. In such a case, the crystallization process involves diffusional atomic jumps across the advancing transformation process. Thus, this type of crystallization is similar to massive transformation in solid-solid reaction and is known as polymorphous crystallization. The growth of the crystalline product is interfacial controlled thus the growth rate is fast in the polymorphous crystallization mode, resulting in relatively gross final microstructure. The polymorphously crystallized phase $\alpha$ with composition a is metastable with respect to the precipitation of second phase c, unless the composition is within the single phase region. If the composition is outside, the precipitation of $\beta$ phase should follow from the polymorphously crystallized $\alpha$. In that case, the final microstructure is comprised of $\beta$ phase particles embedded in the $\alpha$ phase matrix, thus the crystallization reaction of the amorphous phase a occur in two stages:

$$amorphous \rightarrow \alpha \rightarrow \alpha + \beta$$

When the composition of the product phase is different from that of the amorphous phase, crystallization occurs with compositional change. The appearance of the first phase in the first stage of crystallization is determined by the driving force for crystallization of each phase at the composition of the amorphous phase. The amorphous alloy with composition between c and

d is supersaturated with respect to both α and β phases. In such a case, eutectic crystallization occurs, where the alloying elements gets partitioned into two crystalline phases. This requires diffusion at or near to the transformation front and is most frequently observed in amorphous alloys, because stable amorphous alloys tend to have compositions close to the eutectic composition, where the highest glass forming ability is obtained. The amorphous alloy reaches an equilibrium condition after crystallization in the eutectic mode, thus reaching completion in one step. The decomposition with the eutectic mode is thus represented as:

$$amorphous \rightarrow \alpha + \beta$$

The amorphous alloy with the compositions in between the two crystallization modes mentioned above, i.e. compositions between b and c, and d and e, crystallizes with the primary crystallization mode. In Fig. 2.3b, the primary crystal of the α phase with composition c precipitates from the matrix amorphous phase when the amorphous alloy with composition a is crystallized. The composition of the primary crystal, c, is determined so that the chemical driving force for nucleation, ΔG, is the maximum. Assuming a local equilibrium, the composition of the amorphous phase at the α/amorphous interface will be b. This crystallization process is called primary crystallization, and the microstructure obtained by this process is in general very fine because its grain growth is diffusion-controlled. When a solute concentration in the amorphous phase becomes uniform and reaches $X_B$, the volume fraction of the α phase becomes constant and the system reaches the metastable equilibrium between α and the remaining amorphous phase, c-b in Fig. 2.3b. The remaining amorphous phase, b, is still metastable with respect to both α and β phase. Thus, if the alloy is further annealed, the remaining amorphous phase transforms to α and β by eutectic crystallization and the equilibrium state, c–d, is achieved. If the composition of the remaining amorphous phase is close to that of the β phase, the second

crystallization reaction of the remaining amorphous phase will occur by the polymorphous crystallization. Hence, the crystallization process of the amorphous alloy starting with the primary crystallization progresses in two stages:

$$amorphous \rightarrow \alpha + amorphous \rightarrow \alpha + \beta$$

In addition to these three crystallization modes, if thermodynamic conditions are met, phase decomposition may occur in the glassy state prior to the crystallization reaction. However, the phase decomposition in glassy state is possible only when the free energy composition curve of the liquid phase is curved upwards due to a large positive enthalpy of mixing of alloying elements in glassy state.

The thermal stability following elevated-temperature exposure or thermal cycling will be crucial in exploiting the novel structural and functional properties of nanoscale thin films for advanced engineering applications. In this case, however, one has no clue a priori as to exactly what atomic configurations to expect, as there are no known structural arrangements, such as those in the -ΔH compounds, that would provide low-energy states for the alloy.

## 2.4 Three Dimensional Atom Probe Analysis (3DAP)

Physical properties of metallic materials are sensitive to their microstructures. Controlling it by heat treatment, plastic deformation and thermo-mechanical treatment, has been a popular method for improving mechanical, magnetic, and electrical properties of metallic materials. At times the scale of the microstructures reach the nanometer scale; as examples, the nano-scale precipitates in bulk metallic glasses and Guinier Preston zones in high strength aluminum alloys are a few to mention. It has been known for a long time that the strength of materials becomes high when the grain size is refined. The relationship between the strength and the crystal grain size is known as the Hall–Petch relationship, and this has been used as a guiding

principle for developing high strength metallic materials in the past. Characterization of such nano-sized materials becomes very important and atom probe tomography is an extremely powerful and unique technique for 3D atomic level characterization. In this section, crystallization processes, nanocrystalline microstructural evolution in some amorphous alloy systems, is overviewed mainly based on recent atom probe studies.

In 1988, Yoshizawa et al.[40] reported excellent soft magnetic properties with nanometer scale crystals in Fe–Si–B–Nb–Cu amorphous alloy. The alloy ribbons were prepared by single roller method. The microstructure of the alloy consists of the nanocrystalline D03 Fe3Si phase with an average grain size of approximately 10 nm. Yoshizawa et al.[41] reported that a combined addition of Nb and Cu is required for producing such nanocrystalline microstructure, hence the role of Nb and Cu for nanocrystallization has been of great interest. 1DAP[42,43] and 3DAP[44] were used to investigate the role of these additives in the microstructural evolution of an amorphous $Fe_{73.5}Si_{13.5}B_9Nb_3Cu_1$ alloy by crystallization. Three phases are present in the optimally heat-treated nanocrystalline microstructure as shown in Fig. 2.4. The D03 phase contains 20–25 at.%Si with little Nb and Cu. A few atomic per cent of boron remains in this phase, and this appears to be a common feature of the α-Fe particles crystallized from boron containing Fe based amorphous alloys. The remaining amorphous phase is enriched in B and Nb containing a small amount of Si. Since atom probe is sensitive to local compositional change on a nanometer scale, it can detect solute clusters which are formed even prior to the crystallization reaction. 3DAP elemental maps of Cu within the analyzed volumes of 10x10x40 nm in an as-melt-spun specimen annealed for 5 and 60 min at 400°C are shown in Fig. 2.5. Based on extended x-ray absorption fine structure (EXAFS) measurement results, Sakurai et al.[45] and Ayers et al.[46] reported that Cu atoms form clusters having near-fcc symmetry from the very early stage of the

heat treatment. Thus, the Cu clusters observed in the 3DAP data are believed to have a fcc-like short range ordered structure, but they do not appear to be distinct fcc-Cu in the initial stage. Such evidences for nano scale phase separation has been shown in several other systems using 3DAP, for example in $Cu_{43}Zr_{43}Al_7Ag_7$[47], $Fe_{90}Zr_7B_3$[48], $Fe_{89}Zr_7B_3Cu_1$[49],

2.5 Critical Issues Related to Amorphous Phase Formation in Immiscible Systems to be Addressed in this Work

a. Short-range order is a typical characteristic of the amorphous phases formed in systems with negative heat of mixing. These amorphous phases are truly alloyed at the atomic scale and the local atomic arrangements within the amorphous phase often resemble those of the stable equilibrium phases. Due to the substantial local chemical and topological order present in these amorphous alloys, their heats of crystallization are typically of the order of a few kJ/mol.[50] More recently, there have also been reports on amorphous phase formation in systems that exhibit $+\Delta H$ including immiscible systems. In such immiscible systems, the mixing of the constituent elements even in the liquid state is highly unfavorable and results in a substantial increase in the Gibbs free energy of the system. Hence, the reason for the formation of amorphous phases on rapid solidification is not well understood. However, there are two schools of thought to explain the above cause. The first school of thought proposed by Michaelsen et al.[51] is based on the concept that the $\Delta H_{mix}$ of the liquid phase in these immiscible systems is not a constant but a function of temperature. Their argument is based on both experimental and thermodynamic modeling results on the Cu-Nb immiscible system. Based on their experimental observations, Michaelsen et al. proposed that while the $\Delta H_{mix}$ of the liquid is positive at high temperatures, decreases and becomes negative at lower temperatures.

In other words, the strongly clustering tendency of the liquid phase at higher temperatures reduces to an ordering tendency at lower temperatures with bonds between unlike atoms being favored at lower temperatures.[52] Consequently, the enthalpy state of the amorphous phase is lowered and the heat of crystallization is not very large. On the contrary, He et. al.[53,54] have attributed the formation of amorphous phases and its stabilization in the immiscible Ag – Ni system to nanoscale phase separation in the amorphous state. The nanoscale phase separation within the amorphous phase, leading to a non-uniform spinodal-like structure, was cited as the primary reason responsible for the stabilization of the amorphous phase in such immiscible systems.[41,42] From the thermodynamic viewpoint, this nanoscale phase separation reduces the Gibbs free energy of the amorphous phase substantially by forming Ag-rich and Ni-rich regions without the development of any long-range crystalline periodicity. A similar study has been done on the Cu-Nb system in this work and the reason behind the stabilization of the amorphous phase has been presented.

b. In the past few years, there has been a significant increase in the experimental studies of crystallization of amorphous solids. The great interest in these materials is largely due to their increasing applications in modern technology. Their possible applications in the future are large, based on characteristic properties such as chemical reactivity or inertia, electronic-excitation phenomena, soft magnetic properties, superconductivity etc. In that respect, their thermal stability is essential for any application at the sustained elevated temperatures. Crystallization paths followed in the Cu-Nb amorphous alloy system has not been studied in detail until now. Hence, it is very

important to understand the mechanism of crystallization in this system for the aforementioned reasons.

c. Detailed characterization of the amorphous phase in immiscible Cu-Nb has been done using x-ray diffraction, TEM and 3-dimensional atom probe (3DAP). It is very essential to couple the results obtained from each technique as it has been shown that one particular technique is not enough to characterize the thin films deposited by physical vapor deposition. A detailed study on the crystallization kinetics of Cu-45%Nb amorphous film has been done and the results from all the above mentioned techniques have been presented.

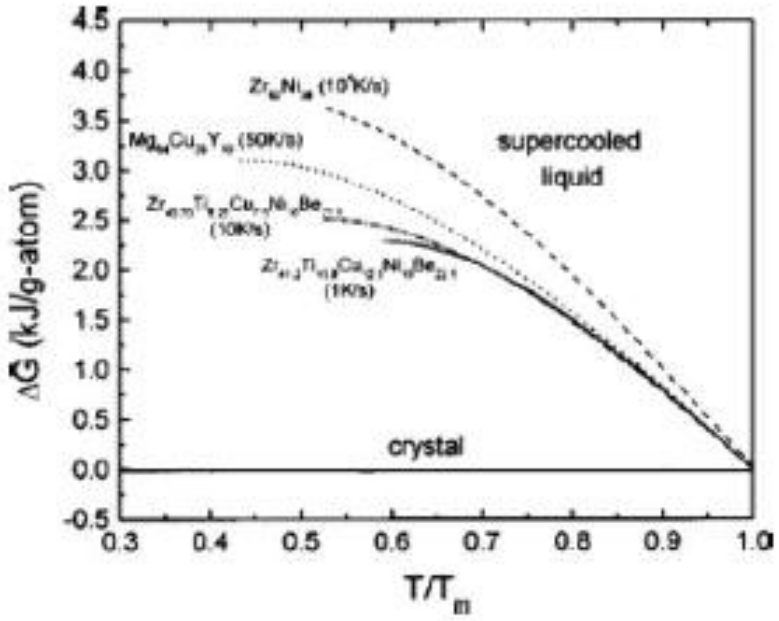


*Fig. 2.1: Gibbs free-energy difference between the undercooled liquid and crystalline mixture for different glass-forming alloys.*[11] *(Copyright 1998, American Institute of Physics. Used by permission.)*

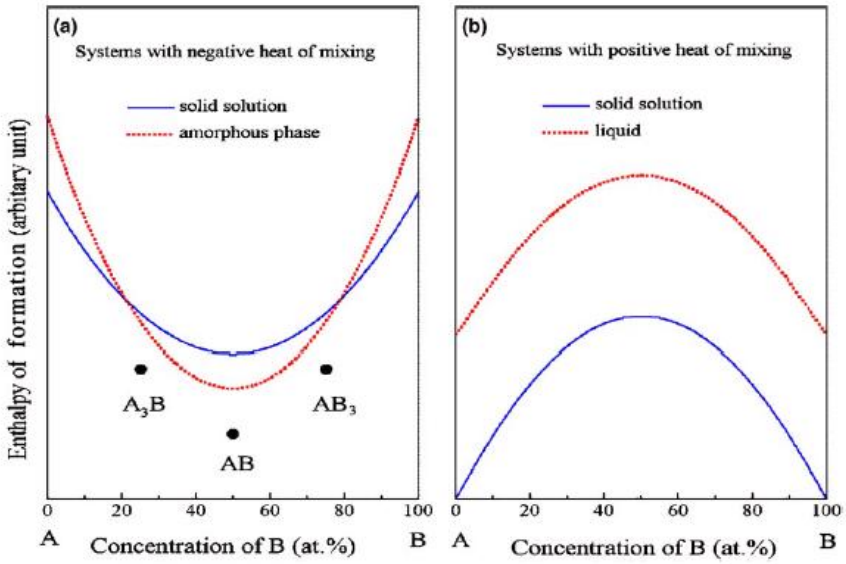


*Fig. 2.2: Schematic illustration of enthalpy-composition comparing systems with a) negative and b) positive heats of mixing .*

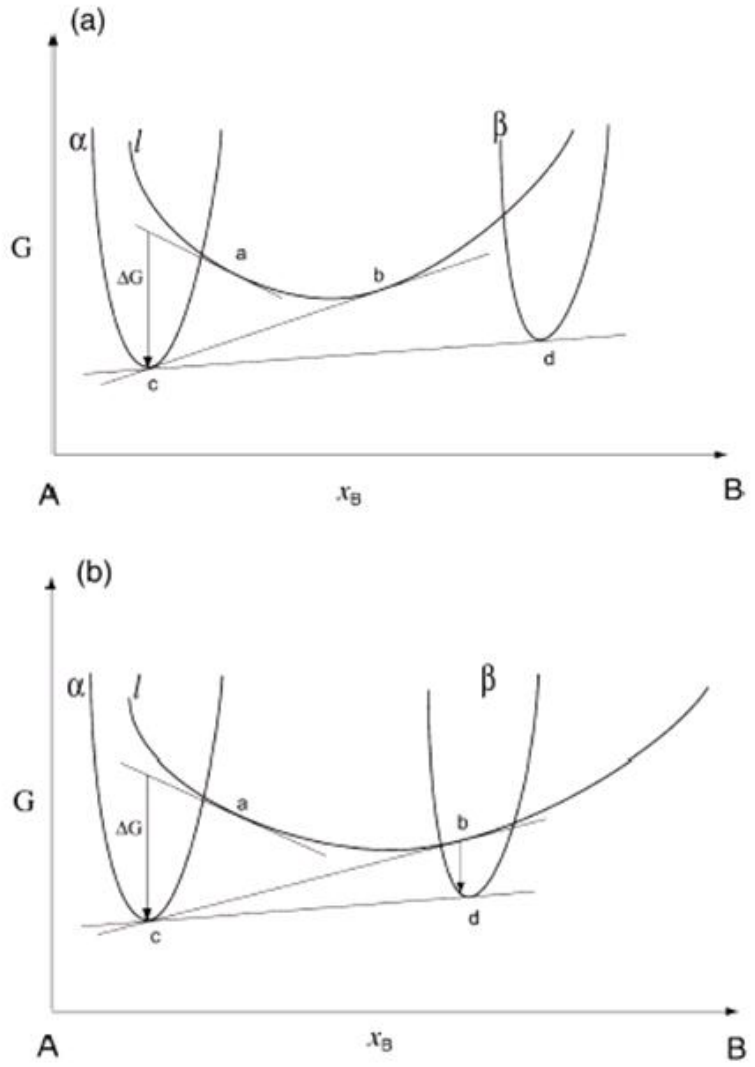


*Fig. 2.3: Hypothetical free energy curve to illustrate modes of crystallization. (Copyright 2002, Elsevier Science Ltd. Used by permission.)*

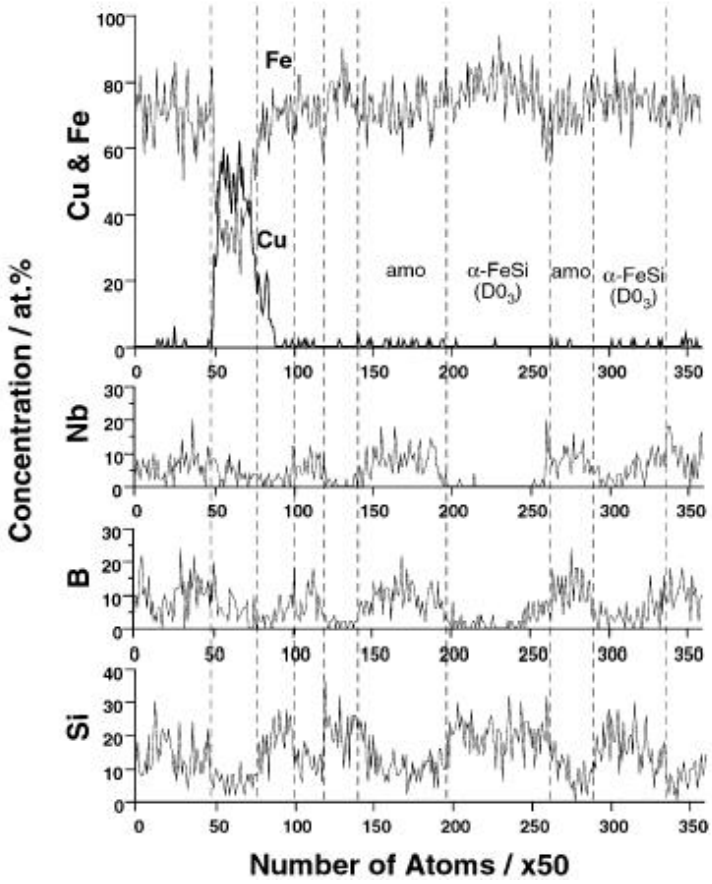


*Fig. 2.4: Atom probe concentration depth profile from $Fe_{73.5}Si_{13.5}B_9Nb_3Cu_1$ alloy annealed at 823K for 60 min.*[55] *(Copyright 2002, Elsevier Science Ltd. Used by permission.)*

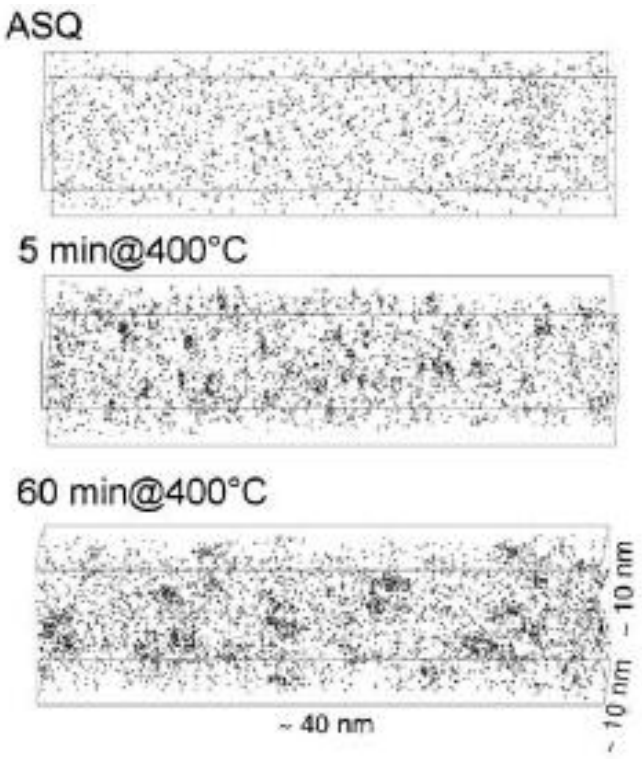


*Fig. 2.5: 3DAP elemental maps of Cu of $Fe_{73.5}Si_{13.5}B_9Nb_3Cu_1$, as-quenched and annealed for 5min and 60 min at 400C.*[55] *(Copyright 2002, Elsevier Science Ltd. Used by permission.)*

# CHAPTER 3

# EXPERIMENTAL

## 3.1 Sample Preparation

### 3.1.1 Sputtering

Sputtering is a physical vapor deposition process whereby atoms in a solid target material are ejected into the gas phase due to bombardment of the material by energetic ions forming plasma. It is commonly used for thin-film deposition technique. Sputtering is largely driven by momentum exchange between the ions and atoms in the material, due to collisions. The number of atoms ejected from the surface per incident ion is called the sputter yield and is an important measure of the efficiency of the sputtering process. The other things that sputter yield depends on are the energy of the incident ions, the masses of the ions and target atoms, and the binding energy of atoms in the solid.

The ions for the sputtering process are supplied by a plasma that is induced in the sputtering equipment. In practice a variety of techniques are used to modify the plasma properties, especially ion density, to achieve the optimum sputtering conditions, including usage of RF (radio frequency) alternating current, utilization of magnetic fields, and application of a bias voltage to the target.

Sputtered atoms ejected into the gas (argon) phase are not in their thermodynamic equilibrium state. Deposition of the sputtered material tends to occur on all surfaces inside the vacuum chamber. Sputtering is used extensively in the semiconductor industry to deposit thin films of various materials in integrated circuit processing. Thin antireflection coatings on glass

for optical applications are also deposited by sputtering. Because of the low substrate temperatures used, sputtering is an ideal method to deposit contact metals for thin-film transistors. Perhaps the most familiar products of sputtering are low-emissivity coatings on glass, used in double-pane window assemblies. The coating is a multilayer containing silver and metal oxides such as zinc oxide, tin oxide, or titanium dioxide.

In the present work, the Cu-Nb alloy thin films were deposited on a Si substrate using a DC magnetron co-sputtering system. Pure elemental Cu (99.99%) and Nb (99.99%) targets supplied by the Kurt Lesker company were used for the depositions. The base pressure prior to sputtering was 5 x $10^{-8}$ torr within the deposition chamber and the pressure of Ar gas maintained during sputtering was 5 x $10^{-3}$ torr. Thin films of composition Cu-45at% Nb were obtained by co-sputtering Cu and Nb at 50W and 200W respectively for 5 hours. In order to explore the atomic scale structure and chemistry of these films, they have been investigated by 3D atom probe tomography. For this purpose, films of composition Cu – 45at%Nb were deposited on flat-top silicon microtip samples. These flat-top silicon microtip samples consist of a 6 x 6 array of silicon micropillars (~ 20μm height and 2μm tip diameter) on a silicon wafer. The microtip samples were then sharpened using the focused ion beam (FIB) to get a sharp tip (~ tip radius of 50-100 nm).

### 3.1.2 Focused Ion Beam (FIB)

FIB systems have numerous and important applications especially for the semiconductor industry. On the analytical side, site-specific sample preparation for scanning and transmission electron microscopes (SEM/TEM) has been so easy and repeatable.

A FIB instrument looks and operates much like a scanning electron microscope (SEM). Both instruments rely on a focused beam to create a specimen image; an ion beam for the FIB

and an electron beam for the SEM. For both instruments, the intensity of the secondary electrons produced at each raster position of the beam is displayed to create an image of the sample. In the FIB, secondary ions may also be detected and used to construct an image of the sample. Images having magnifications up to ~ 100 000 times are available using a FIB with a very good depth of field. The operation of a FIB begins with a liquid metal ion source (LMIS). A reservoir of gallium (Ga) is positioned in contact with a sharp tungsten (W) needle. The Ga wets the needle and flows to the W tip. A high extraction field ($>10^8$ V/cm) is used to pull the liquid Ga into a sharp cone whose radius may be 5–10 nm. Ions are emitted as a result of field ionization and then accelerated down the FIB column. The use of Ga is advantageous for two reasons: (a) Ga has a low melting point and, therefore, exists in the liquid state near room temperature, and (b) Ga can be focused to a very fine probe size (<10 nm in diameter). FIBs typically operate with an accelerating voltage between 5 and 50 keV. By controlling the strength of the electrostatic lenses and adjusting the effective aperture sizes, the probe current density can be varied. The probe schematic diagram of the LMIS and FIB column is illustrated in Fig 3.1. An understanding of the sputtering process is important for a knowledgeable operation of the FIB. When a $Ga^+$ ion is accelerated toward the target sample, it enters the sample and creates a cascade of events which results in the ejection of a sputtered particle (which may be an ion or a neutral atom). This sputtering mechanism thus also results in $Ga^+$ implantation into the sample. The primary ion penetration depth is ~20 nm for 25 keV $Ga^+$. In this study, a Dual Beam Nova 200 FIB system from the FEI company was used to prepare samples for atom probe studies.

## 3.2 Characterization

### 3.2.1 X-ray Diffraction (XRD)

X-Ray diffraction is a non-destructive technique used for the identification of crystalline phases of solid materials and powders. X-ray diffraction can be used to measure the structural properties like stress, grain size, phase composition, crystal orientation and defects of the phases. This method can be effectively used to determine the atomic arrangements in amorphous materials and thickness of the thin films and multilayer thin films. X-ray diffraction has applications in structural analysis, phase analysis, texture analysis and stress measurements. It can be used to determine the crystal structure of a material by comparing its produced diffraction patterns with reference diffraction patterns. In this present work, a Rigaku Ultima III x-ray diffraction is employed for the analysis of the Cu-Nb films in the as-deposited and heat-treated conditions.

X-ray diffractometer uses a beam of x-rays to bombard a specimen from various angles. X-rays are produced in evacuated x-ray tube by directing an electron beam of high voltage at metal anode. Operating voltages depends on the target metal. The x-rays are diffracted as they are reflected from successive planes. The condition where the reflected beams interfere positively to give a strong diffracted beam is given by Bragg's law and it is given by the equation:

$$n\lambda = 2d\sin\theta$$

Where $n$ is an integral number describing the order of reflection, $\lambda$ is the wavelength of the x-rays, $d$ is the spacing between the lattice planes and $\theta$ is the Bragg angle. In x-ray diffraction measurements, the wavelength $\lambda$ is given by the radiation emitted from the x-ray tube hence the $d$ spacing can be easily evaluated from the Bragg's law. The regular arrangement of

atoms in crystal has numerous stacks of parallel lattice planes and each stack has different characteristic *d* spacing. Therefore each crystallographic phase shows a characteristic set of *d* spacings, which yield to a characteristic diffraction pattern with intensities at the corresponding Bragg angles. These diffraction patterns are then identified by comparing them with reference patterns. After the beam has been diffracted from the specimen, it passes through a set of slits, which reduces the radiation of the beam representing different intensities (E. Lifshin, 1999). The position of the peaks depends on the crystal structure of the sample with allowed reflections in fcc and bcc metals. The plot is drawn between intensity and 2θ and these peaks are compared with standard charts to know the crystallographic orientation.

### 3.2.2 Transmission Electron Microscopy (TEM)

Transmission electron microscopy is an imaging technique whereby a beam of electrons is focused onto a specimen causing an enlarged version to appear on a fluorescent screen or layer of photographic film or to be detected by a charge-coupled device (CCD) camera. Electrons are generated by a process known as thermionic discharge in the same manner as the cathode in a cathode ray tube, or by field emission; they are then accelerated by an electric field and focused by electrical and magnetic fields onto the sample. The electrons can be focused onto the sample providing a resolution far better than is possible with light microscopes, and with improved depth of vision. A schematic of TEM is shown in Fig. 3.2.

The contrast in a TEM image is not like the contrast in a light microscope image. A crystalline material interacts with the electron beam mostly by diffraction rather than absorption, although the intensity of the transmitted beam is still affected by the volume and density of the material through which it passes. The intensity of the diffraction depends on the orientation of the planes of atoms in a crystal relative to the electron beam — at certain angles the electron

beam is diffracted strongly, sending electrons away from the axis of the incoming beam, while at other angles the beam is largely transmitted. Modern TEMs are equipped with specimen holders that allow the user to tilt the specimen to a range of angles in order to obtain specific diffraction conditions, and apertures placed below the specimen allow the user to select electrons diffracted in a particular direction. A high contrast image can therefore be formed by blocking electrons deflected away from the optical axis of the microscope by placing the aperture to allow only unscattered electrons through. This produces a variation in the electron intensity that reveals information on the crystal structure, and can be viewed on a fluorescent screen, or recorded on photographic film or captured electronically.

Bright field (BF) imaging is particularly sensitive to extended crystal lattice defects in an otherwise ordered crystal. As the local distortion of the crystal around the defect changes the angle of the crystal plane, the intensity of the scattering will vary around the defect. As the image is formed by the distortion of the crystal planes around the defect, the contrast in these images does not normally coincide exactly with the defect, but is slightly to one side. It is also possible to produce an image from electrons deflected by a particular crystal plane. By either moving the aperture to the position of the deflected electrons, or tilting the electron beam so that the deflected electrons pass through the centered aperture, an image can be formed of only deflected electrons, known as a dark field (DF) image.

In the most powerful diffraction contrast TEM instruments, crystal structure can also be investigated by high resolution transmission electron microscopy (HRTEM), also known as phase contrast imaging as the images are formed due to differences in phase of electron waves scattered through a thin specimen. Resolution of the HRTEM is limited by spherical and chromatic aberration, but a new generation of aberration correctors has been able to overcome

spherical aberration. Software correction of spherical aberration has allowed the production of images with sufficient resolution to show carbon atoms in diamond separated by only 0.89 Angstrom (Å) units and atoms in silicon at 0.78 Å at magnifications of 50 million times. Improved resolution has also allowed the imaging of lighter atoms that scatter electrons less efficiently — lithium atoms have been imaged in lithium battery materials. The ability to determine the positions of atoms within materials has made the HRTEM an indispensable tool for nanotechnology research and development in many fields.

### 3.2.3 Atom Probe Tomography

#### 3.2.3.1 Introduction

Atom probe tomography is an extremely powerful and unique technique for 3D atomic level characterization. Invented by Muller and his coworkers[56] it was originally developed as a tool for studying surface science, and it was further developed and used to solve many critical problems on the microstructures of metallic materials. Soon after, several groups started using atom probe for microstructural characterization of metals. They have been mainly applied to materials where solutes are not distributed uniformly and information regarding solute distribution is required. Typical applications are the early stages of precipitation or phase separation, interphase interfaces, segregation of elements at grain boundaries, clustering and ordering. More recently they have also been applied to a wide variety of materials like semiconductors, thin film single/multi layer deposits and oxide superconductors.

#### 3.2.3.2 Field Ion Microscope

The most widely used atom probe (AP) is a time-of-flight (ToF) atom probe. Atoms are ionized from the surface of the tip of a specimen by applying voltage to a field ion microscope (FIM) specimen. A schematic of the conventional atom probe field ion microscope (APFIM) is

shown in fig 3.3. It is a combination of FIM and a ToF mass spectrometer. Detailed description of the technique can be obtained from references.[57,58,59] Individual atoms can be imaged by field ionization of imaging gas atoms at the sharp sites on the surface of the needle (sample). It has a magnification of approximately one million. The diameter of the FIM tip is approximately 100nm and a high voltage ranging from 1 to 15kV is applied to it. At such high electric fields (20-30V/nm), imaging gas atoms that are introduced into the FIM chamber are ionized by the filed ionization process. It occurs preferentially at the site where the local electric field is high, and they are accelerated towards the microchannel plate (MCP) detector. The FIM image is a projection of atoms protruding at the surface of the FIM specimen. A typical FIM image is shown in fig 3.4.[60] The tip of FIM specimens must have very sharp hemispherical surface to obtain a high electric field of $10^{10}$V/m. for the imaging gas ionization to take place. The electric field of a tip with a radius r is given by F=V/kr, where V is the applied voltage and k is a geometrical factor with a value ranging from 5 to 7.

For example, the ionization field for Ne approximately 40 x $10^{10}$ V/m. To observe a Ne field ion image at an applied voltage of 10kV, the tip radius should be approximately 50nm. Tips with such a radius are usually prepared by electropolishing metal wires or more recently, site specific samples can be prepared on a Si wafer micro-tip using the focused ion beam (FIB). More detailed description on sample preparation is described further down.

3.2.3.3 Traditional Atom Probe

By applying a high voltage pulse of a few tens of nanoseconds, atoms are ionized by the field evaporation phenomena, and the ions go through the probe hole to the detector via an electrostatic reflector called reflectron. The ToFs of the ions evaporated from the tip of the specimen are measured by a time-to-digital converter (TDC). The TDC has a resolution of one

nanosecond. The electrostatic energy of the ion is given by $neV_e$, where n is the number of charge of the ion, e is the charge of the electron and $V_e$ is the voltage of the ion. The atoms are ionized at the total voltage of $V_{dc} + \alpha V_p$, where $\alpha$ is a pulse factor close to unity which vary depending on the transmittance of the pulse to the specimen. The kinetic energy of the ion is given by $\frac{1}{2} mv^2$, hence

$$ne(V_{dc} + \alpha V_p) = \frac{1}{2} m \left(\frac{l}{t-\delta}\right)^2 ,$$

where t is time of flight, $\delta$ is a delay constant and l is flight length. The mass to charge ratio of an ion (m/n) can be measured by rearranging the above equation. Hence the mass to charge ratio can be calculated accurately as long as the time-of-flight is measured accurately. In reality, $V_p$ has some distribution as atoms are not necessarily ionized at the peak of the pulse height, which can cause errors in m/n determined experimentally. To compensate the energy deficit of ions that occur during the pulsed evaporation process, either a Poschenreider lens[61] or a reflectron[62] is installed in the modern atom probes. By using energy compensators the mass resolution ($m/\Delta m$) is improved from less than 100 to a value greater than 500. The data atom probe analysis is done by applying high voltage pulses to a d.c. standing voltage. The analysis is performed at a pulse repetition rate of 200-1000 Hz with a detection rate of 0.05 atom/pulse, meaning approximately 60 atoms are collected per min. The data set of the collected atoms can be converted to a one dimensional depth profile by scaling the depth in proportion to the number of collected atoms. This is 1-dimensional atom probe (1DAP) which is different from 3-dimensional atom probe (3DAP). A 1DAP profile can have an atomic layer resolution when data are collected properly.

The lateral resolution is determined by the size of the probe hole and the evaporation aberration. Evaporation aberration is caused by atomic migration prior to field evaporation,

which occurs because the kink-site atoms on a low index plane migrate to the edge of the lattice plane where they are exposed to higher electric field.[63] Thus even if the tip of the specimen is completely covered by the probe hole, atoms imaged do not necessarily go through the aperture by field evaporation. The physical dimension of the probe hole is 2-3 mm in diameter, which corresponds to about 2-5nm with a magnification of a million. By increasing the distance between the tip and the screen, the selected area can be made smaller. But this increases the error of the depth profile because the number of collected atoms decreases.

Sharp concentration changes from interface can be picked up only if the interface is cut in the normal direction. If it is inclined with respect to the cylinder of analysis, the change in concentration is diffuse when the change in composition is actually different. In addition, the detection efficiency of the atom probe is only about 60%, because the maximum efficiency of a MCP detector is determined by the open area ratio of channels. Thus, the data obtained from atom probe does not contain any information about short range order. But it is sensitive to detect solute clustering in dilute alloys and that depends on the solute concentration in the alloy. The standard deviation for concentrations measured by AP data is given by:

$$\sigma = \sqrt{\frac{x(1-x)}{n}},$$

Where n is the number of atoms and x is the atomic fraction of the solute. It can be found from the above formula that atom probe is quite suitable for detecting clusters of the solute whose concentration is les than a few atomic percent.

3.2.3.4 3D Atom Probe

The three dimensional atom probe (3DAP) combines the magnification of the field ion microscope and in addition to the conventional atom probe information measures x, y coordinates of the filed evaporated ions using a position sensitive detector (PSD). The schematic

of a 3DAP is shown in figure 3.5.[60] It is possible to get two-dimensional elemental information with near atomic resolution by measuring the time of flight and coordinates of the ions using the PSD. Evaporation aberration is the only factor that limits the spatial resolution during the evaporation of atoms. 3D information can be obtained by continuous field evaporation of atoms from the surface of the specimen and reconstructed in a real space. As field evaporation occurs layer by layer in low index planes, if the z coordinate proportional to the number of atoms detected is added to the x, y coordinates (determined by PSD), the reconstructed map in 3D shows the layer corresponding to the atomic planes in the z direction.

The first 3DAP used a wedge and strip type anode as PSD, which is shown in figure 3.6.[64] In font of this a doubly stacked MCP is placed. A shower of secondary electrons is generated when an ion hits the MCP and the charge originating from these electrons are divided into three anodes. The position of the ion can be calculated from the amount of the charge on each anode as given by:

$$x = \frac{Q_1}{Q_1 + Q_2 + Q_3}, y = \frac{Q_1}{Q_1 + Q_2 + Q_3}$$

If two ions hit the detector at the same time, the position of the ions cannot be found out using this method. Hence, the evaporation rate has to be maintained at such a level that the number of multiple hits is minimal. To overcome this, Blavette et al. developed a 3DAP with a multi-hit detection capability[65] : 96 square anodes of 1 x 1 $cm^2$ are placed in a square array of 10 x 10 omitting one from each corner. A triply stacked MCP is placed in front of this. The secondary electrons generated because of an ion hit is measured using a 96 channel charge sensitive ADC as shown in figure 7.[65] Multiple hits of ions can be detected as long as the charges do not overlap. Eight 96 channel charge sensitive ADCs are installed in parallel, each triggered by a different time of flight signals. Hence, ions up to eight different m/ns can be detected from

the evaporation by a single pulse event. Because of the use of a parallel processing system, the data is acquired at a much faster rate than the serial type detector.

Mass resolution capability is very critical in order to distinguish atoms that have their mass to charge ratios closely spaced to each other. For example, $Nb^{3+}$ has m/n equal to 31, $Zr^{3+}$ has a m/n equal to 31.33 and $Cu^{2+}$ has a m/n equal to 31.5 and in order to separate them out a mass resolution higher than 200 is required. In order to improve the mass resolution of 3DAP, Cerezo et al.[66] used a wide acceptance angle reflectron energy compensator in the flight path of the position sensitive atom probe and showed that the information on position can be preserved accurately even when the ions are detected after the energy compensator. Based on this, they developed a prototype energy compensated optical position sensitive atom probe. Figure 3.8 shows a schematic of the system developed by Cerezo et al.[64] A bright spot on the phosphor screen is caused by an ion input and this is transmitted to 32 channel time to digital converter, from which approximate position and accurate time of flight of ions are measured. Accurate position information is obtained using a CCD camera through a half mirror. Detection of multiple hits from a single pulse is possible. A similar system was developed by Deconihout et al.,[67] whose schematic is shown in figure 3.9. In this detector, 16 transparent strips are coated with phosphor. Time of flight signals are detected on these strips, which gives accurate time of flight and approximate positions of the ions. A CCD camera is used to detect accurate positions of atoms.

Interface analysis using a 3DAP is much more accurate and can be done independent of the probe direction unlike the traditional atom probe, where it is impossible to determine the concentration change at the interface without a convolution artifact. With the 3DAP the analysis direction can be selected to be perpendicular to the interface to determine the abrupt change in

the concentration at the interface, which is very difficult using the traditional atom probe, because the interface has to be positioned in an extremely fine needle shaped specimen with a special morphology, the probability of which is very low.

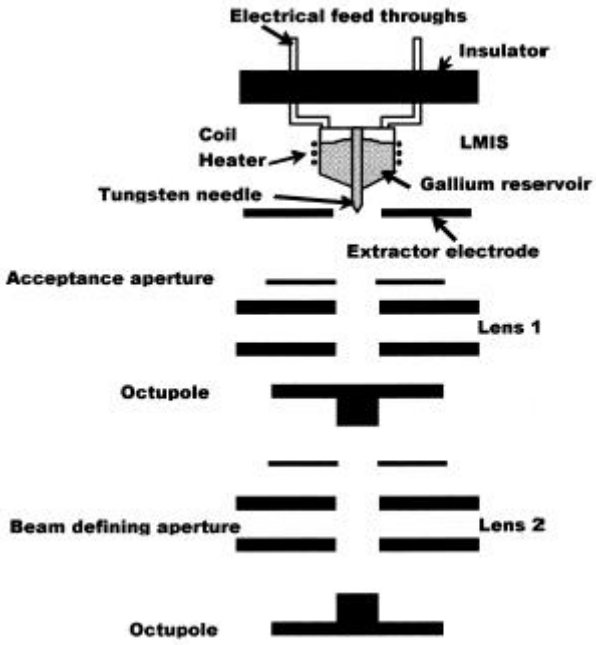


*Fig. 3.1: Schematic of LMIS and the FIB column.*

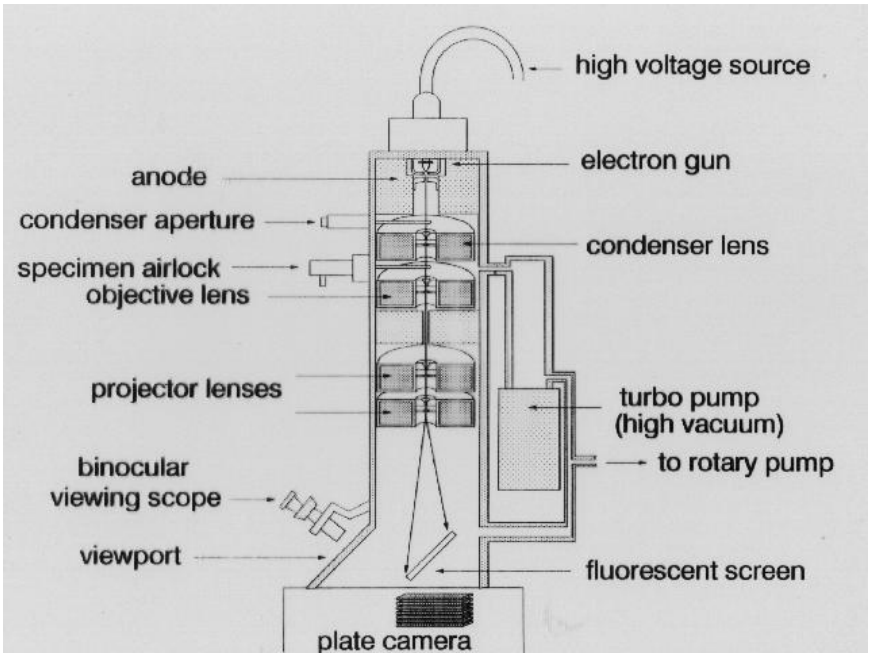


*Fig. 3.2: Schematic of transmission electron microscope.*

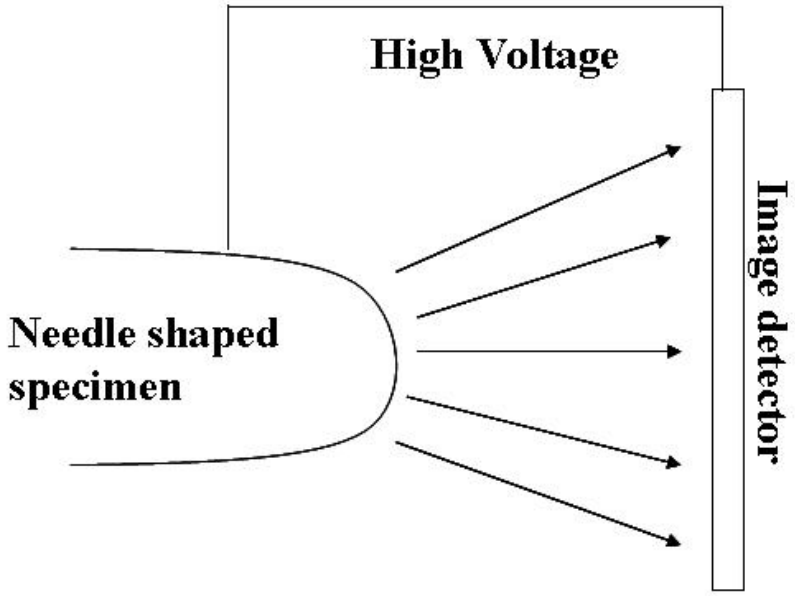


*Fig. 3.3: Basic principle of a field ion microscope.*

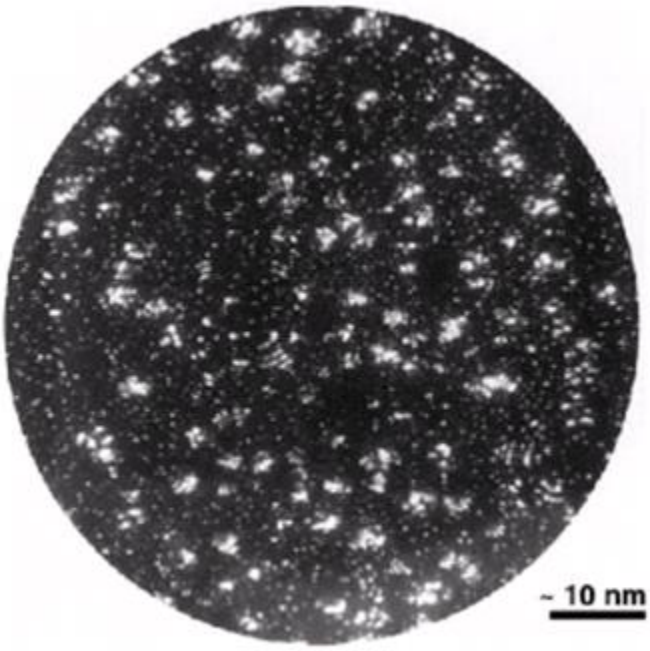


*Fig. 3.4: He field ion image of aluminum.[60] (Copyright 2002, Elsevier Science Ltd. Used by permission.)*

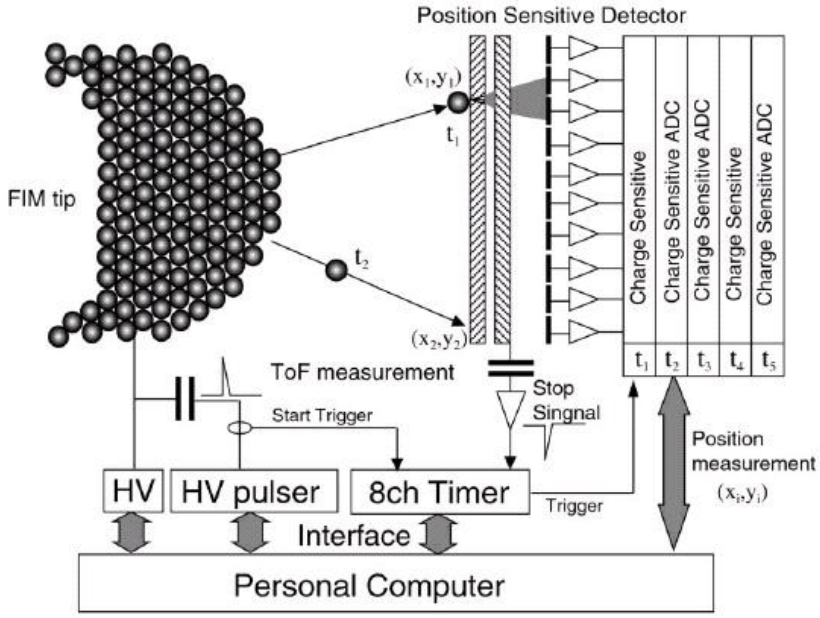


*Fig. 3.5: Schematic illustration of a 3DAP.[60] (Copyright 2002, Elsevier Science Ltd. Used by permission.)*

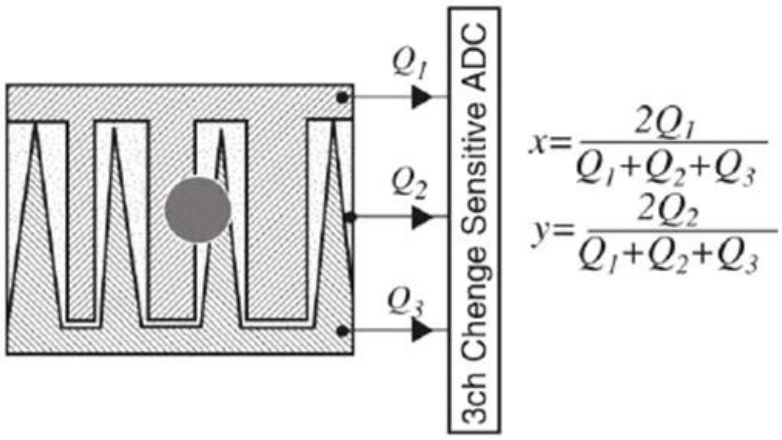


*Fig. 3.6: Schematic of a wedge and strip typed PSD.*[64] *(Copyright 2002, Elsevier Science Ltd. Used by permission.)*

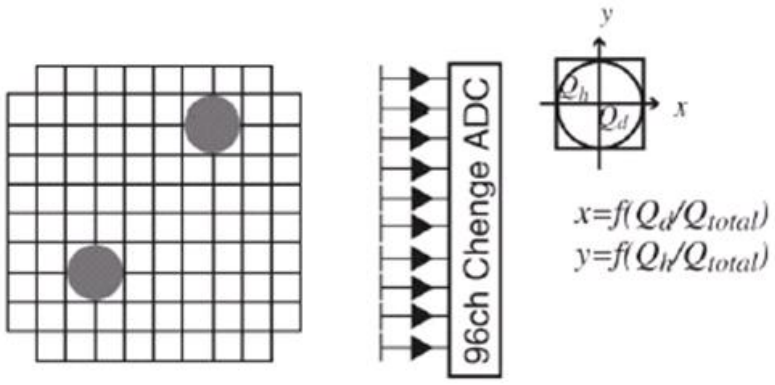


*Fig. 3.7: Schematic of a 96 channel ADC developed by Blavette et al.*[65] *(Copyright 2002, Elsevier Science Ltd. Used by permission.)*

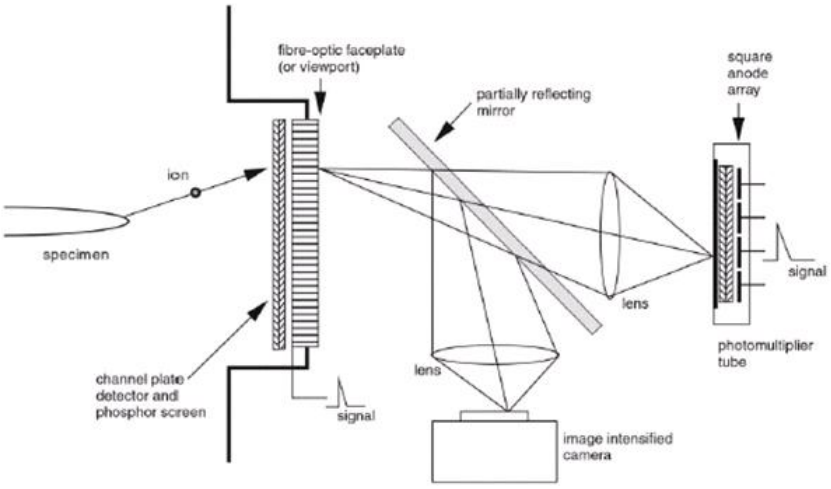


*Fig. 3.8: Schematic of optical position sensitive atom probe.*[66] *(Copyright 2002, Elsevier Science Ltd. Used by permission.)*

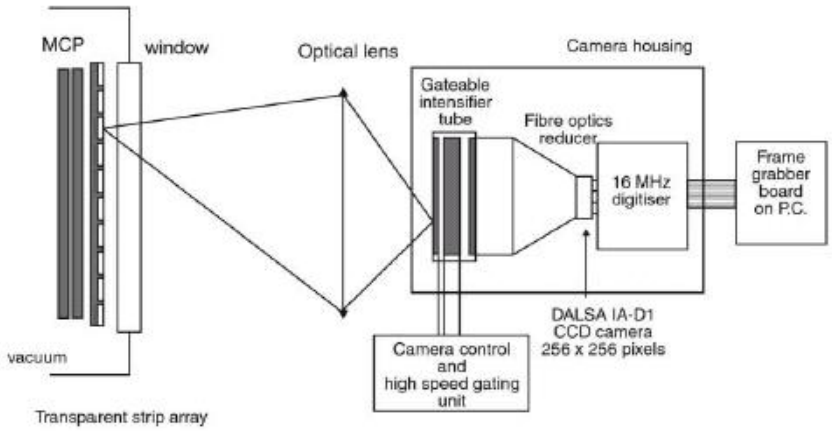


*Fig. 3.9: Schematic of optical tomographic probe developed by Deconihout et al.*[67] *(Copyright 2002, Elsevier Science Ltd. Used by permission.)*

# CHAPTER 4

# RESULTS AND DISCUSSION

## 4.1 Cu-Nb Immiscible Alloy Thin Films – Stabilization of Amorphous Phase

The Cu-Nb immiscible alloy thin films in the amorphous regime have been deposited on Si substrate. The reason(s) for the stabilization of the amorphous phase in these thin films has not been clearly understood. Hence it becomes important to characterize them in a systematic manner. In this study, 3DAP has been used to characterize the atomic arrangements in the amorphous phase. Direct evidence on the atomic arrangements of copper (Cu) and niobium (Nb) in the amorphous phase is presented. Questions like possible phase separation or clustering coupled with the thermodynamic basis for the formation of the amorphous phase has been addressed.

### 4.1.1 Characterization of Amorphous Phase

In the present work, the Cu-Nb system has been re-visited by depositing alloy thin films of this immiscible system using a DC magnetron co-sputtering system. The compositions of these films have been varied by changing the relative deposition rates from the individual Cu and Nb targets via controlling the deposition parameters. Thin films in the composition range 5 – 90 at% Nb have been deposited with the film thicknesses ranging from 2 – 3 nm. The crystallinity and structure of these films have been characterized using XRD and TEM. For compositions in the range of 30 – 70at%Nb the alloy films were found to be amorphous based on the typical amorphous-like features observed in the x-ray diffraction and electron diffraction results. Fig. 4.1 shows XRD results from a Cu-45at%Nb film. A BF-TEM image of the Cu-45at%Nb film is

shown in Fig. 4.2, and the corresponding selected area electron diffraction (SAED) pattern from this film is shown in Fig. 4.3. The SAED pattern shows diffuse halos (rings) consistent with amorphous structures. It should be noted that TEM bright and DF results do not exhibit any strong diffraction contrast features in these amorphous films. It is therefore tempting to conclude that these films are homogenous. Although the results from XRD and TEM establish the lack of any long range order, the chemical homogeneity of these films at the atomic scale cannot be established based on these results or techniques.

In order to explore the atomic scale structure and chemistry of these amorphous films, the films have been investigated using 3D atom probe tomography. For this purpose, films of composition Cu – 45at%Nb were deposited on two types of samples, pre-sharpened silicon microtips and flat-top silicon microtips. These pre-sharpened silicon microtip samples consisted of a 6 x 6 array of silicon micropillars (~ 2μm height and ~ 50 nm tip radius) on a silicon wafer. The flat-top silicon microtip samples consist of a 6 x 6 array of silicon micropillars (~ 20μm height and ~ 3μm tip diameter) on a silicon wafer. X-ray diffraction studies were conducted on these samples to ensure the amorphous nature of these films. Fig. 4.4 shows the thin film on a silicon microtip. In order to be used as an atom probe sample, it was sharpened using a dual beam focused ion beam (FIB) (tip radius ~50-80 nm). Fig. 4.5 is an example of one of the tips after sharpening using FIB. Subsequently, these samples were used for 3D atom probe tomography studies carried out in the local electrode atom probe (LEAP) microscope. No substantial signal from the Ga ions was observed in the atom probe mass spectrum during the evaporation of these sharpened microtips suggesting that the Ga implantation during the ion-beam milling was minimal. Similar results were observed in the case of FIB-prepared atom probe samples of $Cu_{43}Zr_{43}Al_7Ag_7$ bulk metallic glass investigated by Oh et al.[68] Furthermore, in

the present experiments, the atom probe data from both pre-sharpened as well as flat-top microtip samples are identical indicating minimal influence of the sample geometry as well as preparation techniques on the structure and chemistry of these amorphous thin films. For both types of samples, out of the 36 microtips in each case, 10 microtips were evaporated. All atom probe experiments were conducted in the electric-field evaporation mode with the evaporation rate maintained at ~ 0.2% and the pulsing voltage was maintained at 30% of the steady-state applied voltage. 3D reconstructions of the atomic positions of Cu and Nb atoms are shown in Figs. 4.6a and 4.6b. In these images each sphere represents a single atom (or ion). Blue spheres correspond to Cu atoms while the red ones correspond to Nb atoms.

It is evident from this image that the distribution of the Cu and Nb atoms in these amorphous alloy films is not homogeneous. Rather there is a strong tendency for clustering of Cu and Nb atoms resulting in the local formation of Cu-rich and Nb-rich clusters. The scale of this clustering is extremely refined, of the order of a few nanometers. Furthermore it should be noted that the nanoscale clustering of Cu and Nb atoms does not necessarily lead to individual, distinctly separated clusters, but rather an interconnected network of Cu-rich and Nb-rich regions (in a non-crystallographic spinodal-like fashion). A more clearer 3D rendition of this aspect is shown in Fig. 4.6c wherein the Cu-isosurface (regions with Cu >= 70at%) has been plotted in blue and the Nb atoms as red spheres. Two different compositional profiles, across this film are shown in Figs. 4.7a and 4.7b. These compositional profiles are averages over a cylindrical pipe of diameter 2 nm placed diametrically across the 3D reconstruction of the amorphous Cu-Nb film. The compositional inhomogeneity in the amorphous film is evident from these profiles. Since there is no crystallography associated with these profiles of the amorphous film, it is not possible to assign any specific periodicity to the compositional modulations. Rather it is only

possible to define an average modulation width of ~ 2 – 3 nm from the compositional profile. The amplitude of these modulations is also not the same across the spatial extent sampled in Fig. 6c. The maximum compositional variation observed in this sampled volume is from 75at%Cu – 25at%Nb to 25at%Cu – 75 at%Nb. However, since these compositions are averaged over a cylindrical diameter of 2 nm, the values may not reflect the exact compositional variations. It should be noted that the extremely refined scale of this phase separation (~ 2 – 3 nm) did not permit resolving these compositional modulations using high-resolution TEM based techniques, including Z-contrast stem imaging. Subsequent annealing of the amorphous thin films resulted in further coarsening of the Cu-rich clusters and eventually formed crystalline *fcc* Cu precipitates in a Nb-rich amorphous matrix which could be resolved in high-resolution TEM studies.

### 4.1.2 Stabilization of Amorphous Phase – Thermodynamic Aspects

Based on this direct experimental evidence of a nanoscale clustering tendency within the amorphous Cu-Nb phase, the stabilization of this amorphous phase can be discussed. Thus, the enthalpy (H) of the competing amorphous (or liquid), *fcc* solid solution, and, *bcc* solid solution phases in the Cu-Nb system can be computed based on a simple solution thermodynamics based CALPHAD approach[69] and have been plotted as a function of composition in Fig. 4.8. In this case the enthalpy of the amorphous phase has been simply estimated based on a low temperature extrapolation of the enthalpy of the liquid. The plot shown in Fig. 4.8 corresponds to a temperature of 25°C (298 K). The convex shapes for all three enthalpy curves are indicative of the strong clustering tendency in both liquid and solid phases in this system. The enthalpy of the homogeneous amorphous phase of composition 55at%Cu-45at%Nb would correspond to the point marked H1 in Fig. 4.8. This is a very high value of enthalpy and consequently highly unstable state. By phase separating into Cu-rich and Nb-rich regions the system can substantially

lower its enthalpy (and consequently its free energy, G) to as low as a value of H2 (shown on Fig. 4.8). Thus, nanoscale phase separation, driven by the reduction in the enthalpy (and consequently the free energy), is responsible for the stabilization of the amorphous phase in this immiscible alloy system. Consequently for all compositions lying between approximately 20at%Cu to 80at%Cu, phase separation in the amorphous phase can lead to a lower enthalpy of the amorphous phase as compared with the competing crystalline *fcc* phase. Thus, the composition range 20 – 80 at% Cu is amenable for the formation of the amorphous phase in this system. It is important to note that these computations of the free energies for the different competing phases should only be taken as first order approximations since the solution thermodynamic models employed are very basic and largely empirical in nature. In addition to the computed enthalpy plots for the three different phases, Fig. 4.8, also contains the experimentally measured enthalpies of crystallization for amorphous Cu-Nb films of different compositions, based on the data reported by Michaelson et. al.[70] These experimentally measured crystallization enthalpies, from differential scanning calorimeter (DSC) measurements, appear to be substantially lower than the values predicted by the simple CALPHAD model for a phase separated Cu-Nb amorphous phase. However, the trend in the experimentally measured values is very similar to that expected for a phase separated amorphous phase. The differences between the magnitudes of these enthalpy values can possibly be attributed to local topological ordering within the amorphous phase. Thus, while the amorphous phase is compositionally phase separated at the nanoscale, structurally it is likely that topological ordering and occurrence of ordered clusters of atoms, resembling for example, *fcc*-like packing is present. The presence of these topologically-ordered clusters in the amorphous phase substantially lowers its enthalpy as compared to a liquid of similar composition[71,72,73] and could be the underlying reason for the

lower experimentally observed enthalpies of crystallization. Furthermore, in a system such as Cu-Nb with a large mismatch between the atomic radii of the constituent elements, strain energy contributions can be quite substantial for the crystalline *fcc* and *bcc* solid solution phases. The strain energy contributions have not been included in the CALPHAD models used for the *fcc* and *bcc* phases in the present paper. Nevertheless, these first order computations of the free energies for the various phases are still very useful in terms of providing an insight into the competing phase stabilities and also point towards the preferred path adopted by the system for reducing its free energy.

This section gives direct evidence of the nansocale phase separation present within the amorphous phase in immiscible alloy systems. Based on the 3D atom probe tomography results from the amorphous Cu-Nb alloy thin films it can be concluded that there is a nanoscale phase separation (or clustering) within the amorphous phase. As postulated previously by He et al.[5,6] for the case of amorphous Ag-Ni alloy thin films, such a nanoscale phase separation can substantially reduce the Gibbs free energy of the undercooled liquid and consequently stabilize the amorphous phase in these immiscible systems. Therefore, even in case of the Cu-Nb system, the stabilization of the amorphous phase can be attributed to the nanoscale phase separation occurring in this phase. Michaelson et al.[3] suggested a temperature dependent $\Delta H_{mix}$ (liquid) resulting in the change from a clustering to an ordering tendency in the undercooled liquid (or amorphous phase) with a decrease in temperature, for explaining the stabilization of the amorphous phase in immiscible Cu-Nb alloy films. However, it appears that it is the local nanometer-scale clustering tendency within the amorphous phase that is actually responsible for the stabilization of the amorphous phase in this system.

### 4.1.3 Cu-Nb Immiscible Alloy Thin Films – Composition(s) Outside the Amorphous Range

From the above discussion we can approximate a composition range for the formation of amorphous phase. Deviations from it should result in the formation of a single phase, fcc (Cu-rich composition) or bcc (Nb-rich composition) solid solution upon rapid solidification. In order to verify, we deposited thin films in both extreme cases. The first film that was deposited was rich in Cu and its composition was approximately Cu-5%Nb and the second film that was deposited was rich in Nb and the composition of it was approximately Cu-90%Nb. Fig. 4.9 shows a BF-DF pair from the Cu-5%Nb thin film. Fig. 4.10 is the corresponding SAED and the micro-diffraction pattern from the crystals and they correspond to the lattice spacing of fcc Cu. It shows that these films form a supersaturated fcc solid solution with nanocrystalline Cu present throughout the film with a grain size averaging ~50nm. Similar study on the Nb rich film reveals a supersaturated bcc solid solution with grain size averaging ~100nm. Fig 4.11a shows a BF TEM microstructure with the inset revealing a polycrystalline diffraction pattern whose d-spacing were found to be those of bcc Nb and Fig. 4.11b shows the corresponding DF image.

## 4.2 Crystallization of Cu-Nb Immiscible Alloy Thin Films

The previous section shows evidence for nanoscale phase separation in amorphous Cu-Nb alloy thin films. To date, however, there have been no reports on the crystallization path of these types of amorphous films. Whether the nanoscale phase separation in the amorphous condition has any role in the crystallization on annealing is an important question that is addressed in this section. Obviously, it is important from a fundamental point of view and will also be crucial in exploiting the functional properties of these types of films.

### 4.2.1 Heat-treatment Procedures

In this study, the amorphous film was heat-treated at 200°C for three hours, followed by 350°C for three hours in the sputtering chamber under a vacuum of 5 x $10^{-6}$ torr. The thin films deposited on the silicon microtips for atom probe analysis were also heat-treated along with the amorphous film. The crystallinity and structure of the films have been characterized using x-ray diffraction and TEM. A small portion of the film was peeled off the Si wafer and ion milled for TEM analysis. The as deposited film was finally heat treated at 390C for 4.5 hours in the sputtering chamber under a vacuum of about 2 x $10^{-7}$ Torr. During the heat-treatment procedure, the film came off the Si wafer and hence x-ray diffraction could not be done on the thin film. Hence, the film could only be analyzed in TEM after ion milling and the results are presented below.

### 4.2.2 Crystallization in Cu-Nb Immiscible System – Results from 200°C Annealing

After the 200°C anneal the x-ray diffraction pattern (Fig. 4.12) displays an amorphous peak similar to that of the as-deposited film. However, a bright-field TEM image (Fig. 4.13a) of the same film and a high-resolution TEM image (Fig. 4.13b) indicate that the film contains small precipitates surrounded by an amorphous matrix. The corresponding SAED pattern from this film (Fig. 4.14) indicates that the structure contains fine fcc crystallites with a lattice parameter similar to that of pure copper. Dark field images taken using different sections of the 111 fcc ring of Cu (Fig. 4.15) indicate that the precipitates are approximately spherical and range from 3 - 9nm in size with an average size of ~6 nm. The fine size of the particles and the shadow of the broad amorphous peak near the $d_{111}$ X-ray peak could be the reason for not seeing a significant peak for Cu in the x-ray diffraction. 3DAP of these samples reveals small (3-10nm) Cu rich precipitates (Fig. 4.16) consistent with TEM data. Compositional profiles through these

reconstructions indicate that these fcc precipitates contain approximately 90%Cu-10%Nb (Fig. 4.17).

### 4.2.3 Crystallization in Cu-Nb Immiscible System – Results from 350°C and 390°C Annealing

After the 350°C anneal, the x-ray diffraction pattern contained sharp crystalline peaks (Fig. 4.18) at 2θ=38.96°, which corresponds to the 110 of Nb and a minor peak at 2θ=43.36° which corresponds to the 111 of Cu. There is also a small peak at 2θ=32.8°, which is from the Si substrate and can be ignored. The peaks corresponding to fcc Cu and bcc Nb indicate the presence of both precipitates. TEM analysis (Fig. 4.19) revealed that the film was mostly crystalline, although it still contained small amorphous regions with the fine fcc Cu crystallites. The microstructure of the crystalline regions displayed different morphologies, but the majority appeared largely spherulitic and uniformly distributed. The compositions of the large spherulitic crystals were examined using energy dispersive spectrometery (EDS) in the TEM and found to be close to the matrix composition, i.e., Cu-45%Nb. The size of these crystals ranged from 0.5μm – 2μm, with a large fraction of them >1μm. An SAED from one of these spherulites (Fig. 4.19), can be indexed as $<111>_{bcc}$ pattern with some weaker fcc spots lined up with the bcc reflections. A complete set of BF and BF images (Fig. 4.20) were taken from a smaller Nb crystal which was caught at its early stages of growth and shows that Cu is embedded within them. This is confirmed by the 3DAP reconstructions (Fig. 4.21), where the Cu-isosurfaces with Cu >= 70% have been plotted. Indeed, the material contains Cu-rich regions within the niobium grains (Fig. 4.22). Bright field TEM micrographs (Fig. 4.23) from the film heat-treated at 390°C and BF-DF pair (Fig. 4.24) from Nb and Cu reflections, shows Nb and Cu precipitates.

## 4.3 Discussion

TEM and atom probe reveals that the film is not amorphous upon annealing at 200°C. It also confirms that the fine precipitates that form during the low temperature anneal are fcc Cu, showing that Cu precipitates prior to Nb. Michaelsen et al.[3] have also seen Cu precipitating ahead of Nb upon annealing in their insitu x-ray diffraction measurements, although they did not show any experimental evidence. Although, the formation of bcc Nb is thermodynamically favorable or stable, kinetics allows the formation of fcc Cu. The formation of Cu phase has also been observed in the Cu-W system before the formation of most stable phases.[74] As already noted, the as-deposited amorphous Cu-Nb films are phase separated with clusters of Cu and Nb with an average cluster size of 2-3 nm, to start with. The nano-sized Cu rich regions presumably act as nuclei for Cu and being an easy diffuser, this leads to the fine *fcc* Cu precipitates prior to bcc Nb precipitation. Their size indicates that they are primary crystals that form a compositionally modulated amorphous matrix. Hence, it can be said that at low temperatures, the amorphous phase starts forming primary crystals of *fcc* Cu, with the amorphous matrix being enriched in Nb. With respect to free energy, the initial condition of the as-deposited film shows nanoscale phase separation or clustering of two amorphous phases A1 and A2 (Fig. 4.25), where A1 is 75%Cu-25%Nb and A2 is 35%Cu-65%Nb. Hence, the free energy of the as-deposited film is at G1 (Fig. 4.25). At 200°C, the transformation proceeds as described below.

$$A1 + A2 \rightarrow primary(fcc1) + A3$$

, where A3 (Fig. 4.26) is the Nb enriched amorphous phase of composition 45%Cu-55%Nb. This brings down the free energy of the system from G1 to G2 (Fig. 4.26).

At 350°C, the morphology of the film looks completely different, with the formation of a large phase in the shape of spherulite. Thus it is proposed that, with an increase in temperature,

Nb, which is enriched in the remaining amorphous matrix starts nucleating heterogeneously and grows very rapidly. During its growth process, the large *bcc* crystals appear to engulf the fine Cu crystallites. The diffraction pattern (Fig. 4.19b) clearly shows the presence of both phases within the large crystal. The DF images (Fig. 4.21) shows clear evidence that the Cu crystals are trapped within the large *bcc* spherulites. The composition of the large crystal (from EDS) is similar to the matrix (Cu-45%Nb). From the size and the composition of the crystal it can be said that the growth of the crystal is polymorphic in nature. The compositional profiles of the film annealed at 350°C (Fig. 4.22) from 3DAP reconstructions are averages over a cylindrical pipe of diameter 2 nm placed diametrically across the 3D reconstruction of the film annealed at 350°C. Note that there are regions enriched with Cu, within the large *bcc* spherulites and the compositions of Cu reach as high as 92%. In addition, there is still significant supersaturation of Cu in the *bcc* crystals. Unlike the primary crystals that look spherical, the regions enriched in Cu appear to be elliptical (Fig. 4.21), possibly secondary *fcc* precipitates from the supersaturated *bcc* crystals. At 390°C, it appears that the transformation is near completion, as can be seen from the increased size of the Cu precipitates and the domain like structure of the Nb. The proposed transformation path after the 350°C anneal can be summarized as:

primary fcc1 + A3 → primary *fcc*1 + polymorphic *bcc* crystals + secondary *fcc*2

The free energy after the 350°C anneal decreases from G2 to G3 (Fig. 4.27). To prove that the presence of secondary *fcc* precipitates, high resolution tem is used. The primary *fcc* precipitates forms from the phase separated amorphous matrix and they are spherical in morphology. Hence, there is no orientation relationship (OR) expected with the *bcc* matrix. However, the secondary precipitates that forms from the supersaturated *bcc* phase and tend to exhibit an OR with the *bcc* matrix. The high resolution tem images (Fig. 4.28) within a large *bcc*

spherulite shows two different *fcc* precipitates. The fast Fourier transform (FFT) from the region (inset in Fig. 4.28) reveal weak diffraction spots along with the strong *bcc* reflections. Inverse FFT from the weak spots reveal two different *fcc* precipitates (Fig. 4.29a and 4.29b). A higher magnification from the two precipitates (Fig. 4.29c and 4.29d) clearly shows that the secondary fcc precipitate (Fig. 4.29d) has an OR with the *bcc* matrix that is given by:

(110)bcc//(111)fcc, [001]bcc//[-101]fcc

It is similar to the Nishiyama-Wasserman (NW) relationship for *fcc* and *bcc* crystals. Although the FFT (Fig. 4.30) does not reveal this exact OR, it can be seen clearly in Fig. 4.19. The diffraction spot from *fcc* is offset by ~6°, which is also consistent with the NW relationship.

Nanocrystallization microstructures have been known to evolve from various amorphous alloys by the primary crystallization mechanism.[75] In the case of Fe-Si-B-Nb-Cu base nanocrystalline magnetic alloys, the phase decomposition occurs in the amorphous phase to form Cu-rich clusters, which act as nucleation sites for primary crystals.[76] In this study it was confirmed that there is strong clustering tendency for Cu and Nb atoms by 3DAP observations, similar to that shown in the Ag-Ni system.[5,6] They act as quenched in nuclei and grow on heating to form nanocrystalline Cu. Previous studies in bulk forming amorphous alloys suggests that nanocrystalline microstructure evolve either by the occurrence of prior phase decomposition in the amorphous phase or by the existence of short range ordering. A good example would be Zr-Cu-Al-Pd alloy.[77] Although Zr-Cu-Al alloy does not show nanocrystalline microstructure after crystallization, the size of the crystallized microstructure is drastically reduced by the addition of Pd. But it was found out that Pd does not partition into any phases after crystallization and hence its concentration was uniform even after crystallization. Fan et al.[78] attributed the nanocrystal formation tendency in the above system to the tendency of short range ordering due to strong

negative mixing enthalpy of Zr and Pd atoms. In the case of Cu-Nb prior clustering tendency in the amorphous phase plays a vital role in the formation of nanocrystalline microstructure. Moreover, the crystallization of the amorphous film happens below the calculated crystallization temperature of 450°C.[3]

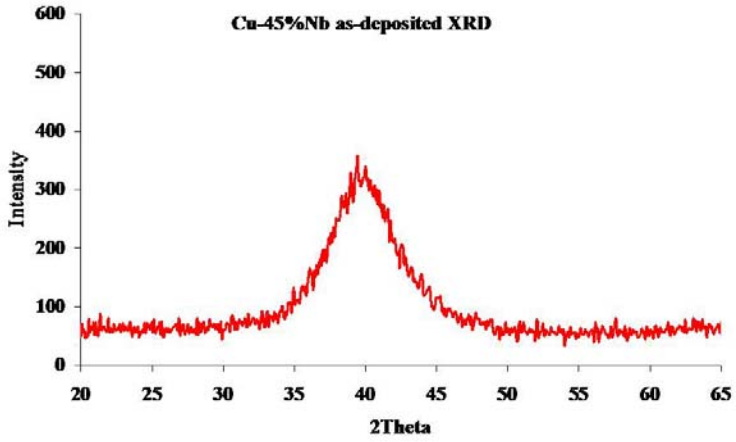


*Fig 4.1: X-ray diffraction of as-deposited Cu-45%Nb film.*

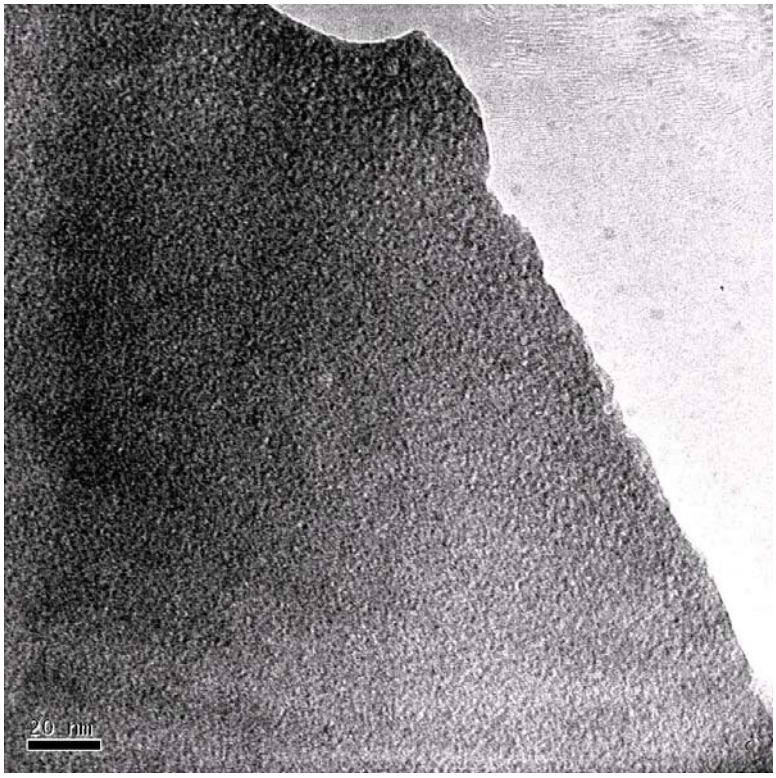


*Fig. 4.2: Bright field TEM of the Cu-45%Nb thin film.*


*Fig. 4.3: SAED from the Cu-45%Nb thin film.*

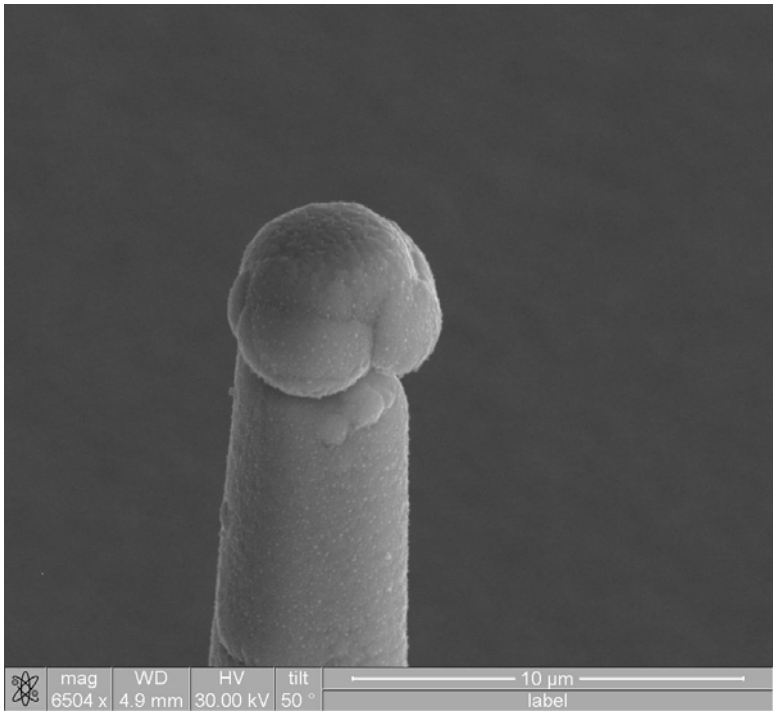


*Fig.4. 4: Thin film deposited on the silicon microtip.*

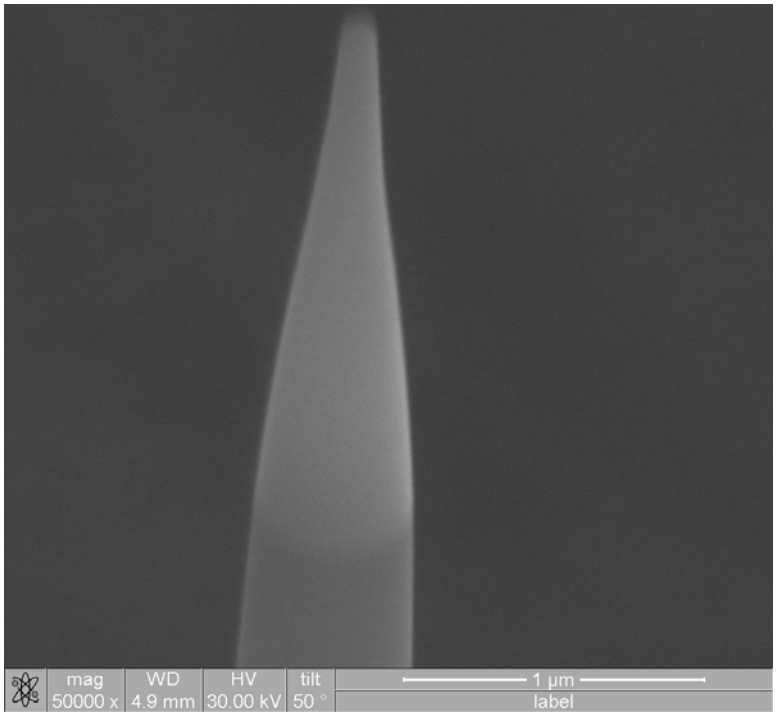


*Fig. 4.5: FIB sharpened atom probe sample of Cu-45%Nb thin film.*

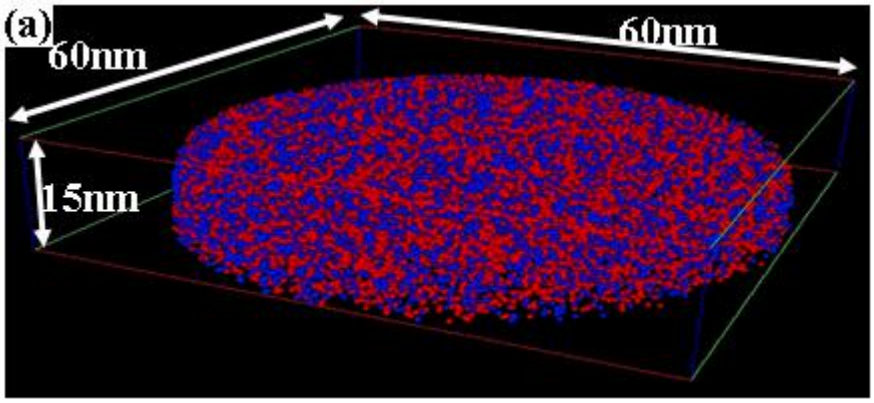


*Fig. 4.6a: 3DAP reconstruction showing Cu(blue) and Nb(red) atoms.*

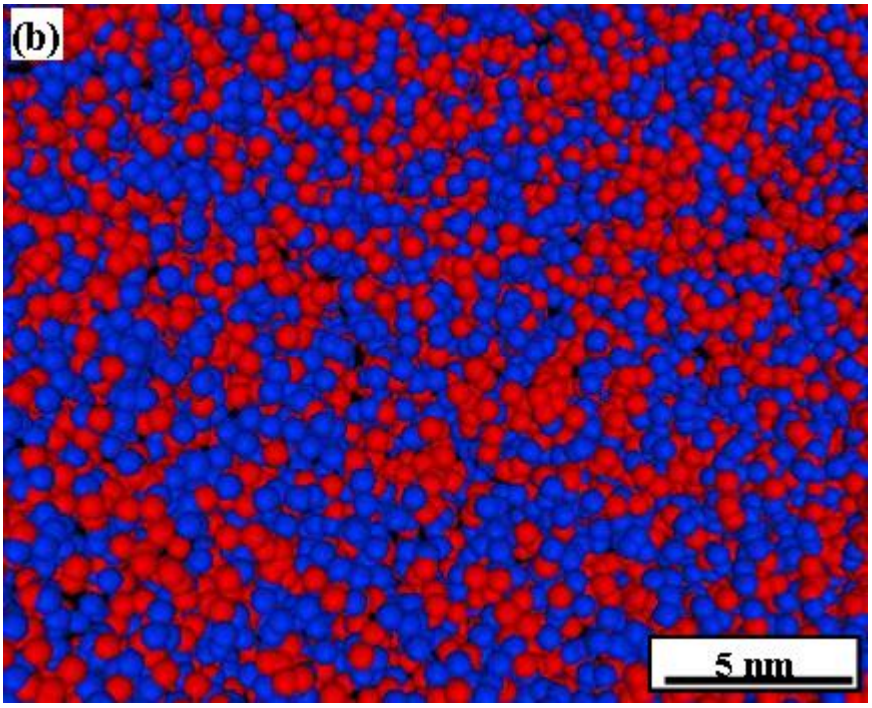


*Fig. 4.6b: Atom probe reconstruction from Cu-45%Nb showing clustering of Cu and Nb atoms.*

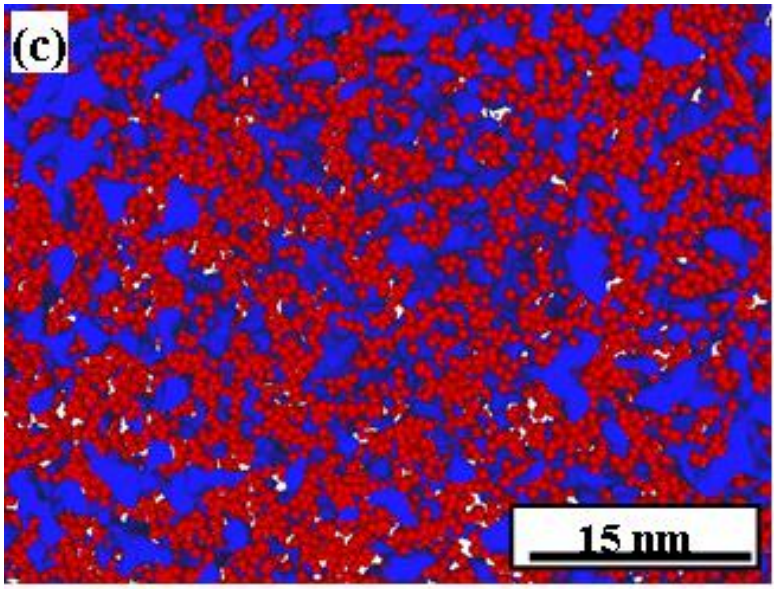


*Fig. 4.6c: 3DAP reconstruction of Cu-45%Nb with Cu isosurface (Cu>=70%) and Nb atoms.*

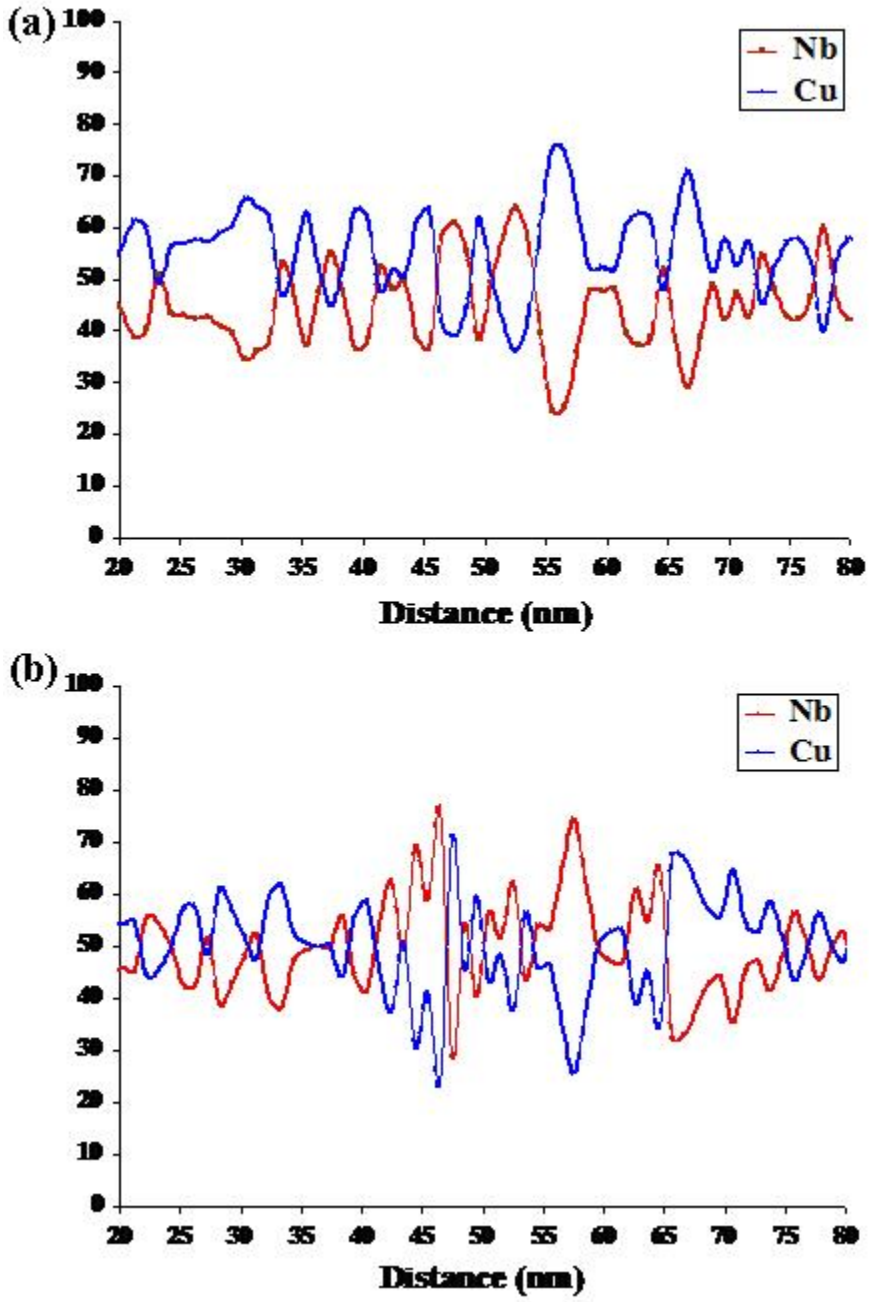


*Fig. 4.7 a and b: Compositional profile showing Cu and Nb clustering of ~2-3nm.*

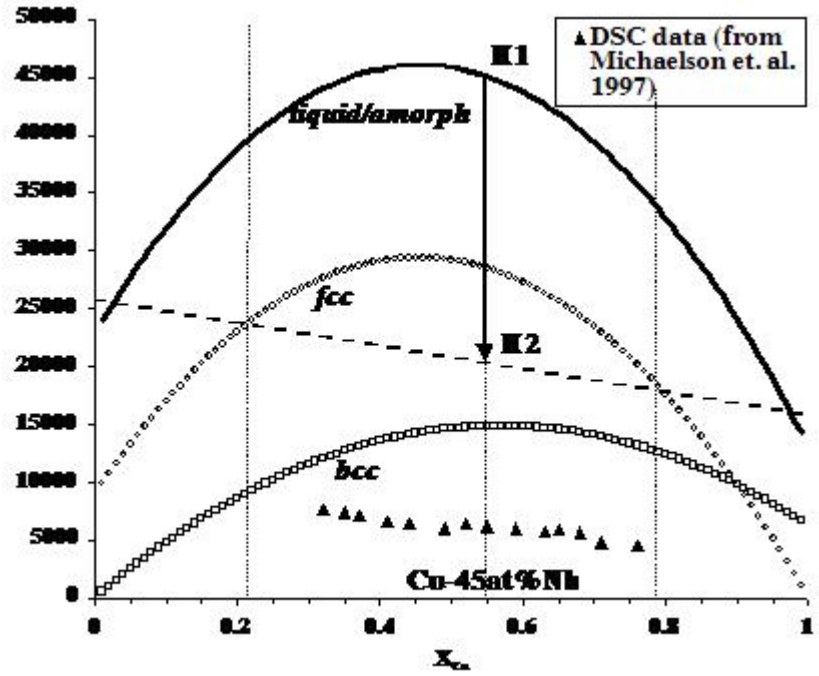


*Fig. 4.8: Enthalphy (H) versus composition (atomic fraction of Cu) plots for the amorphous (extrapolated liquid), fcc solid solution, and, bcc solid solution phases in the Cu-Nb system.*

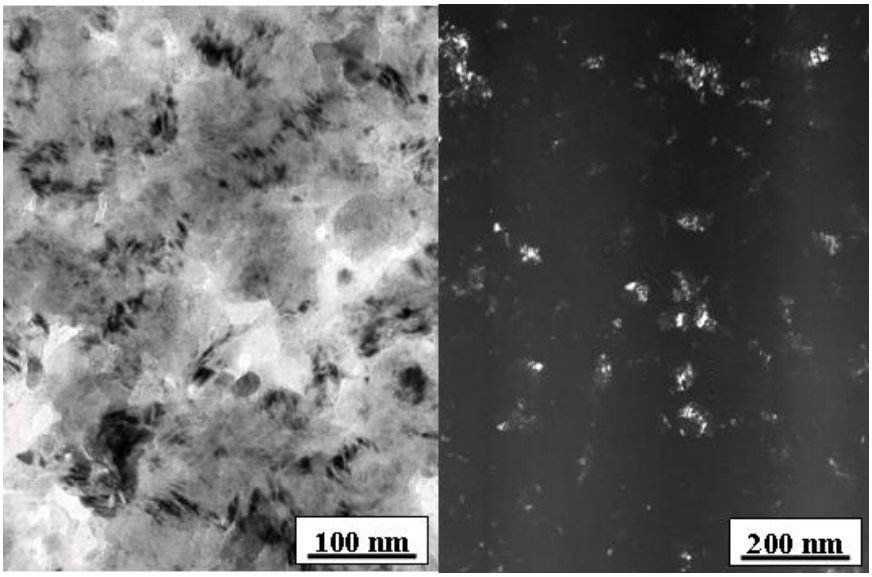


*Fig.4.9: BF-DF pair from Cu-5%Nb thin film in the as-deposited condition showing Cu precipitates ~50nm.*

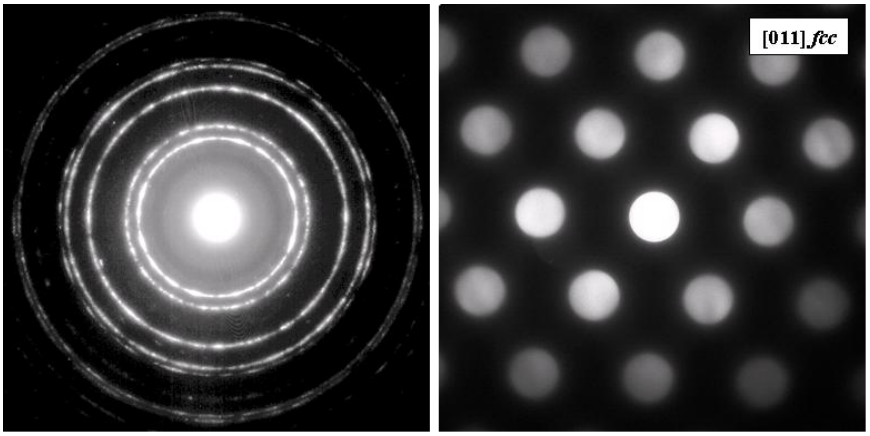


*Fig. 4.10: (left) SAED from the Cu-5%Nb thin film were indexed to be fcc Cu and (right) microdiffraction from one of the fcc Cu precipitates.*

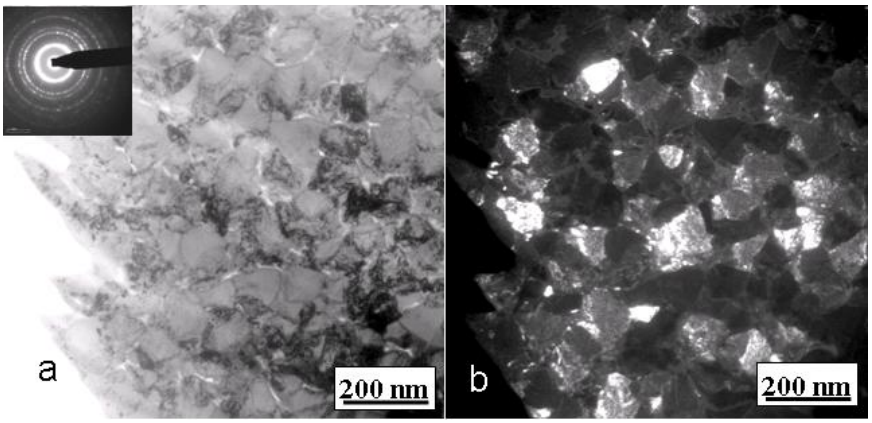


*Fig. 4.11: BF-DF pair from Cu-90%Nb thin film in the as-deposited condition showing Nb. precipitates ~100nm. Inset in 11a is the SAED indexed as bcc Nb.*

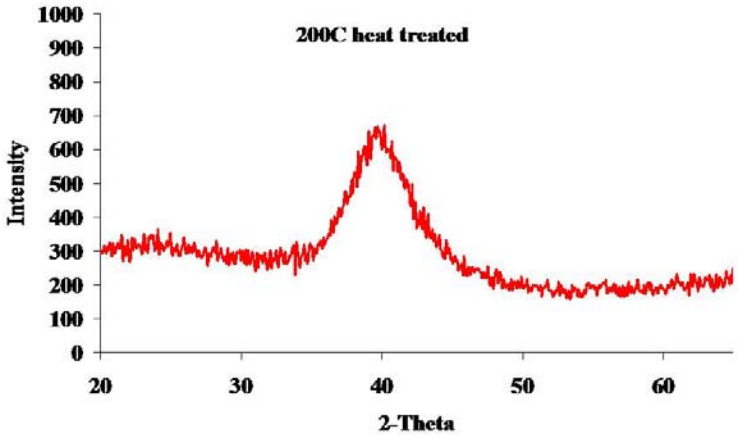


*Fig 4.12: X-ray diffraction of Cu-45%Nb film heat-treated at 200°C.*

(a)

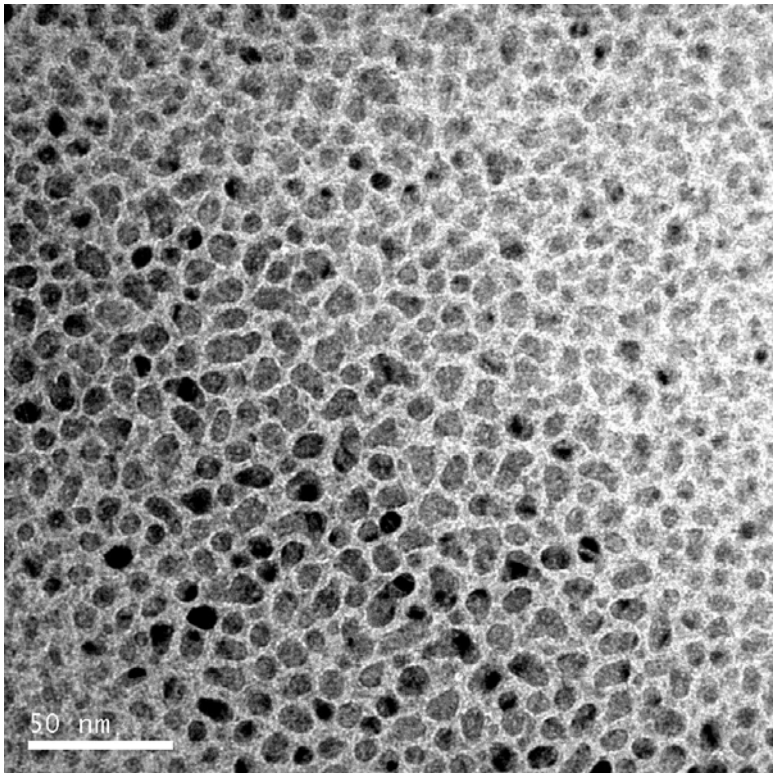


(b)

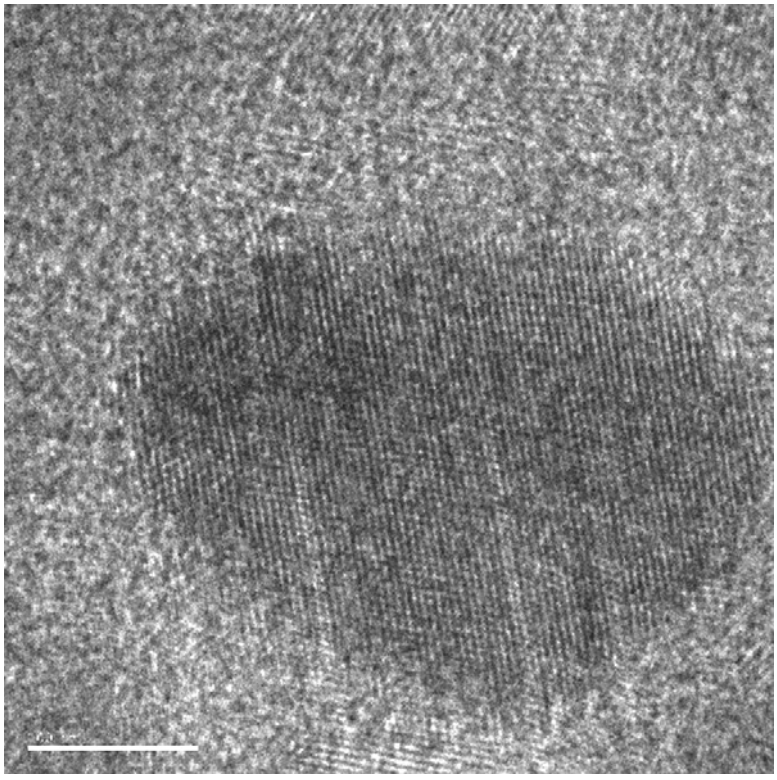

*Fig 4.13: a)BF of Cu-45%Nb film heat-treated at 200°C and b) HRTEM image of Cu precipitate.*

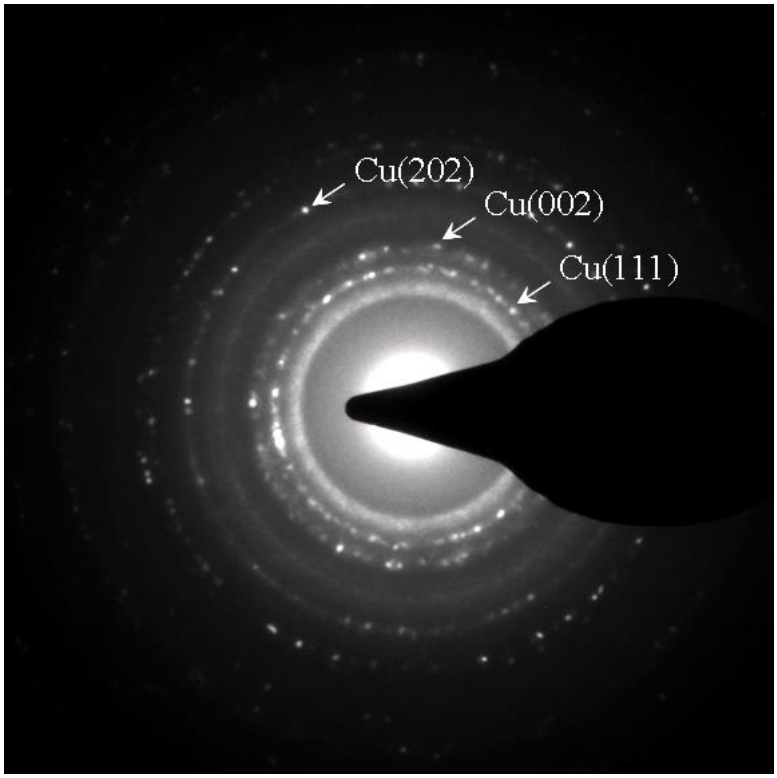


*Fig 4.14: SAED of Cu-45%Nb film heat-treated at 200°C.*

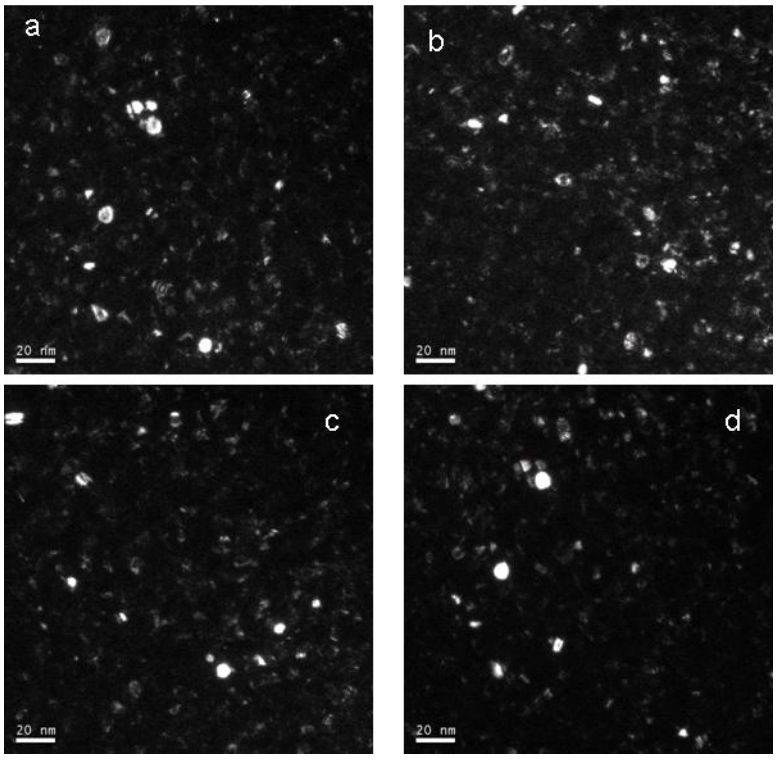


*Fig 4.15: DF from different places around the $d_{111}$ Cu ring shown in fig 4.14.*

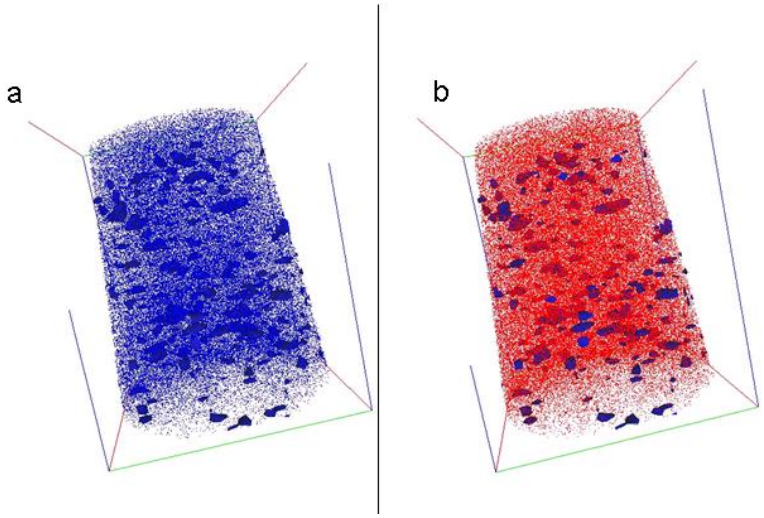


*Fig 4.16: 3DAP reconstruction of Cu isosurface (Cu>=70%) with a)Cu ions and b) Nb ions.*

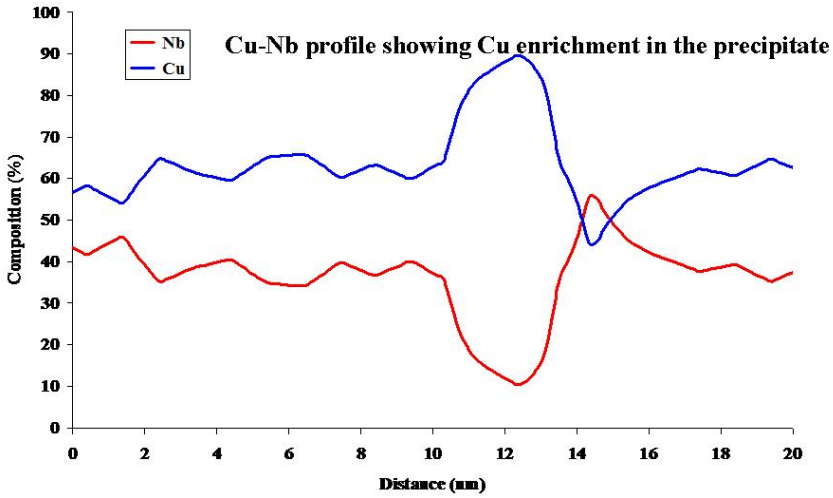


*Fig 4.17: Compositional fluctuation showing Cu enrichment in the precipitates.*

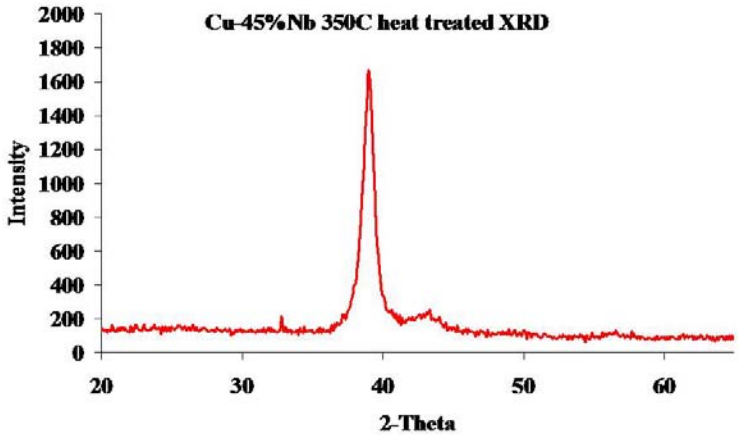


*Fig 4.18:* X-ray diffraction *of Cu-45%Nb film heat-treated at 350°C.*

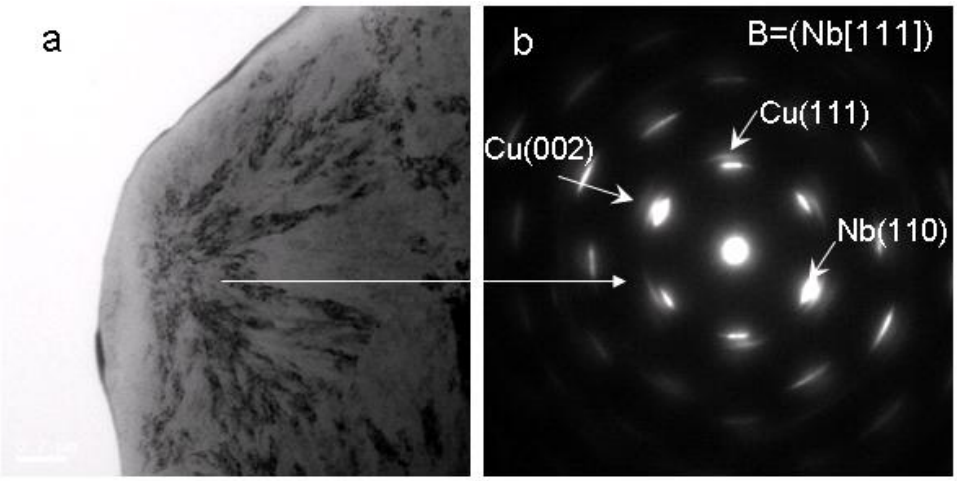


*Fig 4.19: a) BF-TEM and b) SAED of Cu-45%Nb film heat-treated at 350°C.*

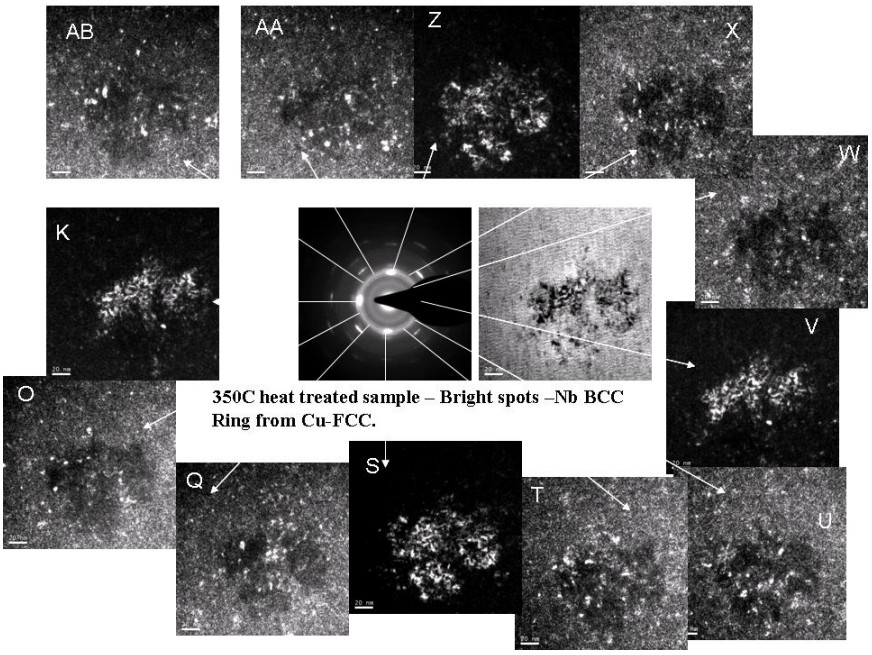


*Fig. 4.20: BF-DF pairs showing Cu precipitates embedded within the larger crystal of Nb.*

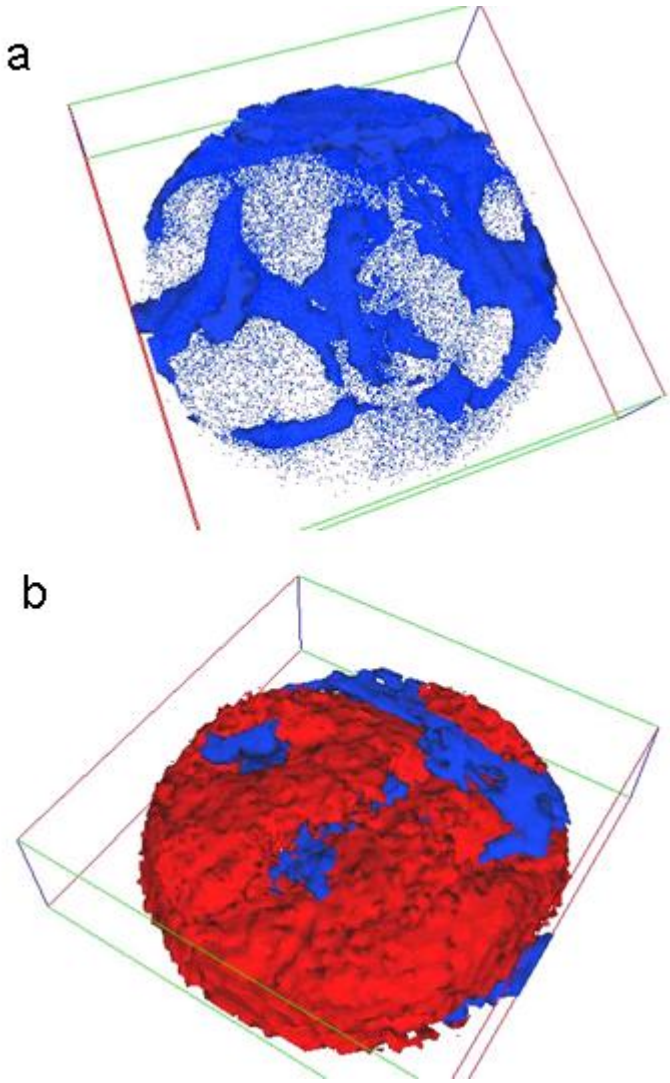


*Fig 4.21: 3DAP reconstruction of 350°C heat-treated film showing a) Cu isosurface with Cu ions and b) Cu and Nb isosurface.*

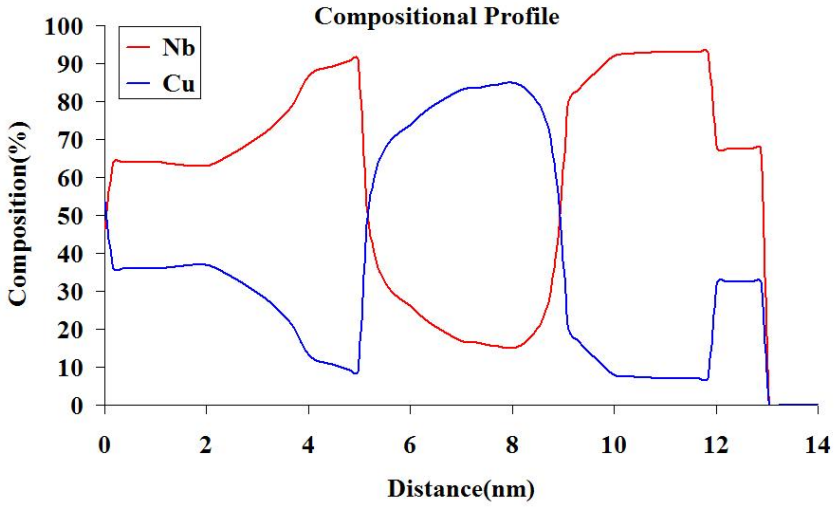


*Fig. 4.22: Compositional fluctuation showing enrichment of Cu and Nb in the form of layers.*

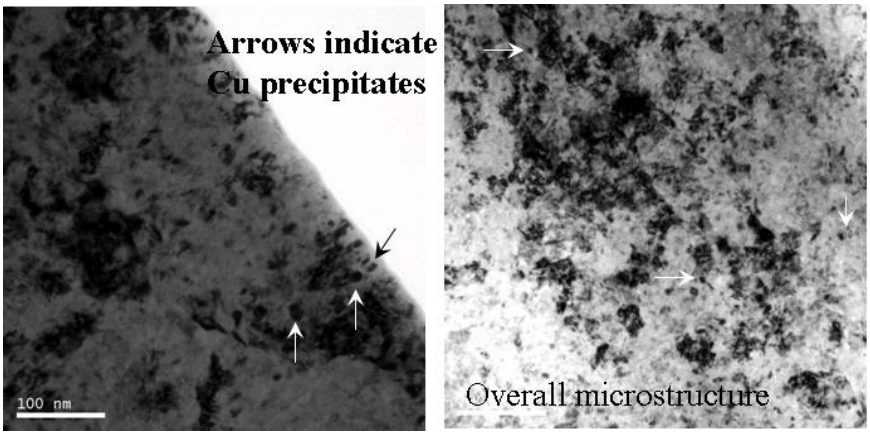


*Fig. 4.23: BF-TEM micrographs from 390°C heat-treated thin film. Arrows indicate Cu-precipitates.*

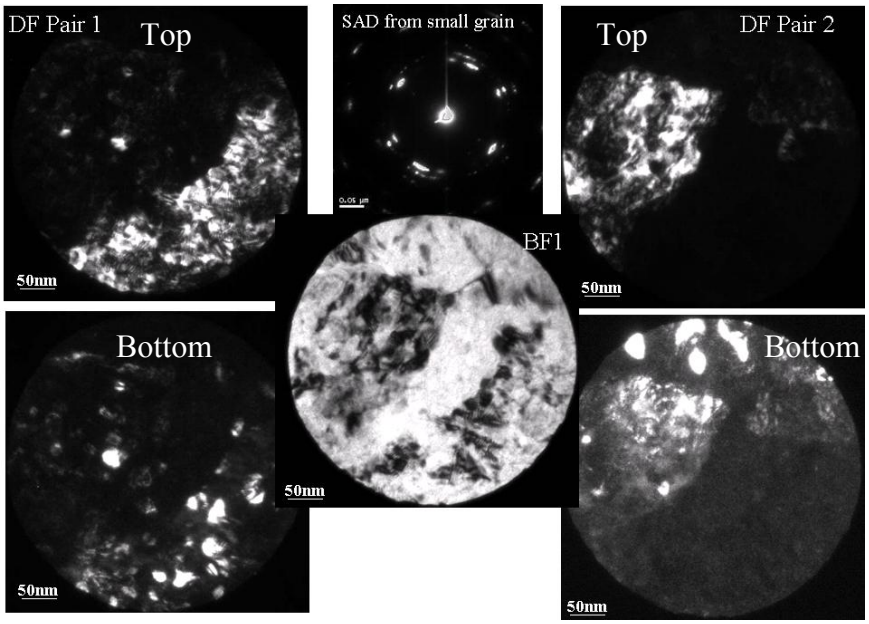


*Fig. 4.24: BF-DF pair from the 390°C heat treated sample. SAED shows reflections from bcc Nb and fcc Cu. The images labeled* Top *shows DF from a Nb reflection and the images labeled* Bottom *shows DF images from two different Cu reflections.*

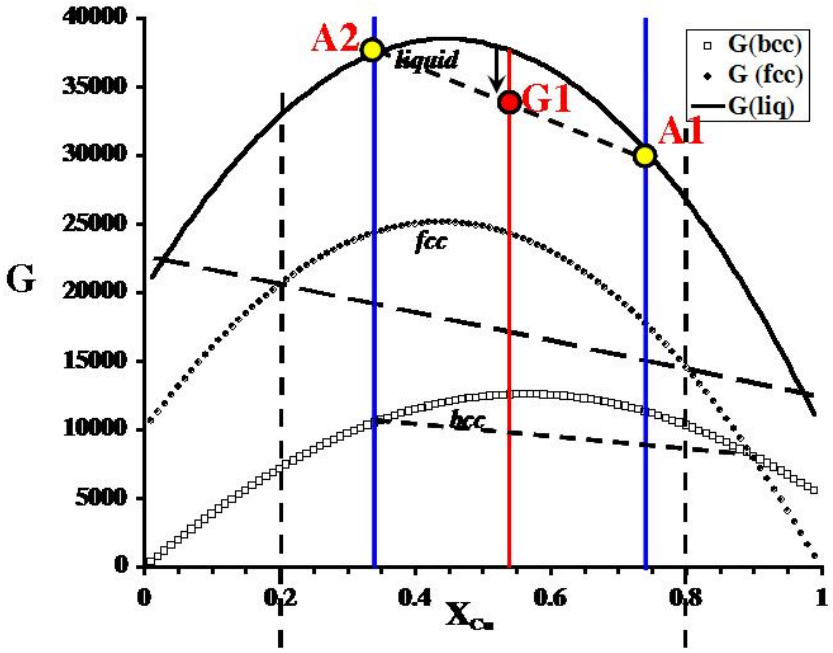


*Fig. 4.25: Free-energy (G) versus composition (atomic fraction of Cu) plots for the amorphous (extrapolated liquid), fcc solid solution, and, bcc solid solution phases in the Cu-Nb system.*

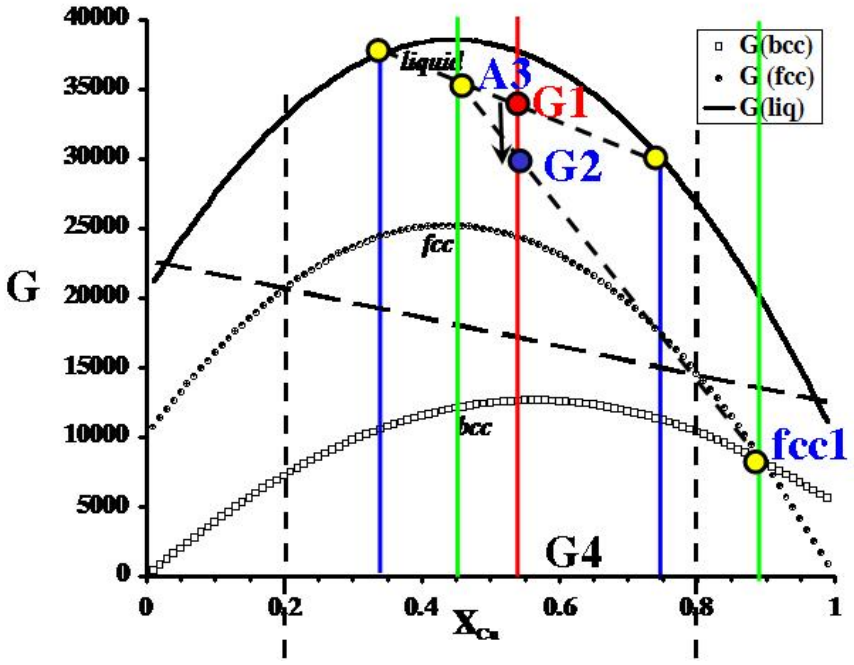


*Fig. 4.26: Free-energy (G) versus composition (atomic fraction of Cu) plots for the film after 200°C anneal.*

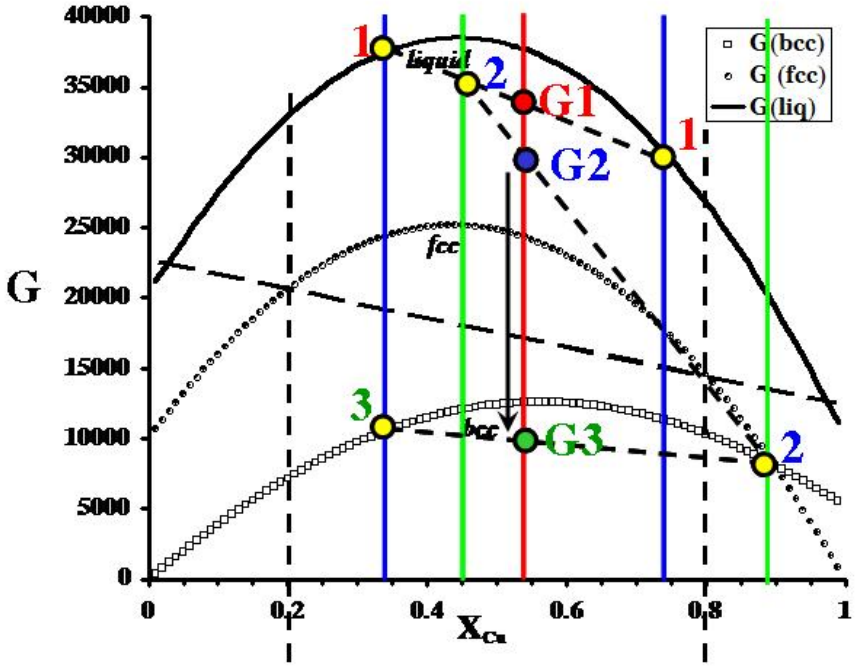


*Fig. 4.27: Free-energy (G) versus composition (atomic fraction of Cu) plots for the film after 350°C anneal.*

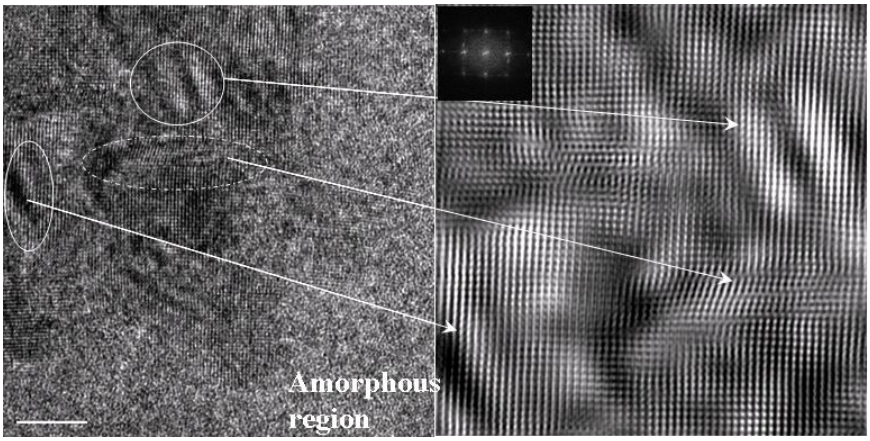


*Fig. 4.28: HRTEM image from the bcc phase showing the two different fcc precipitates (*fcc*1 and* fcc*2). Inset is an FFT of the* fcc *and* bcc.

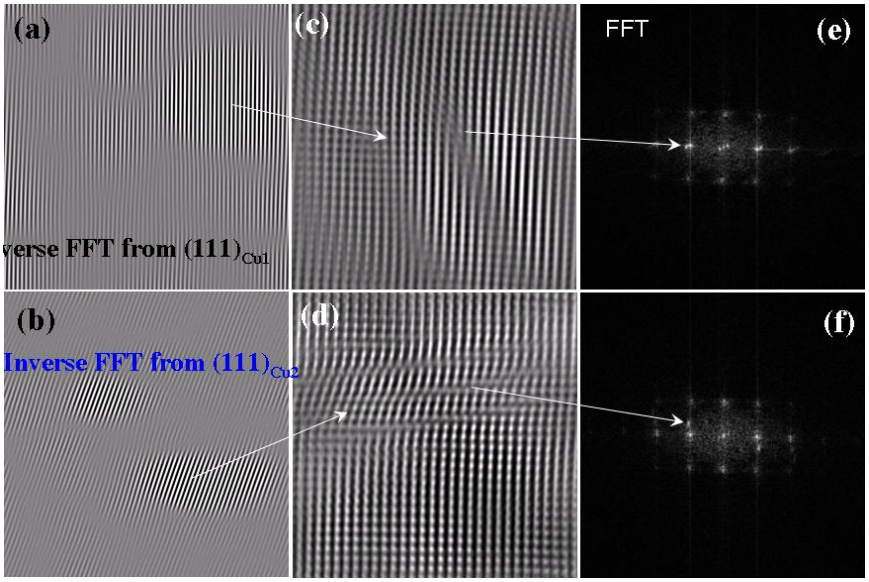


*Fig. 4.29: a & b) HRTEM images (c) showing no OR between* fcc*1 and* bcc *matrix and (d) showing NW OR between* fcc*2 and* bcc *matrix.*

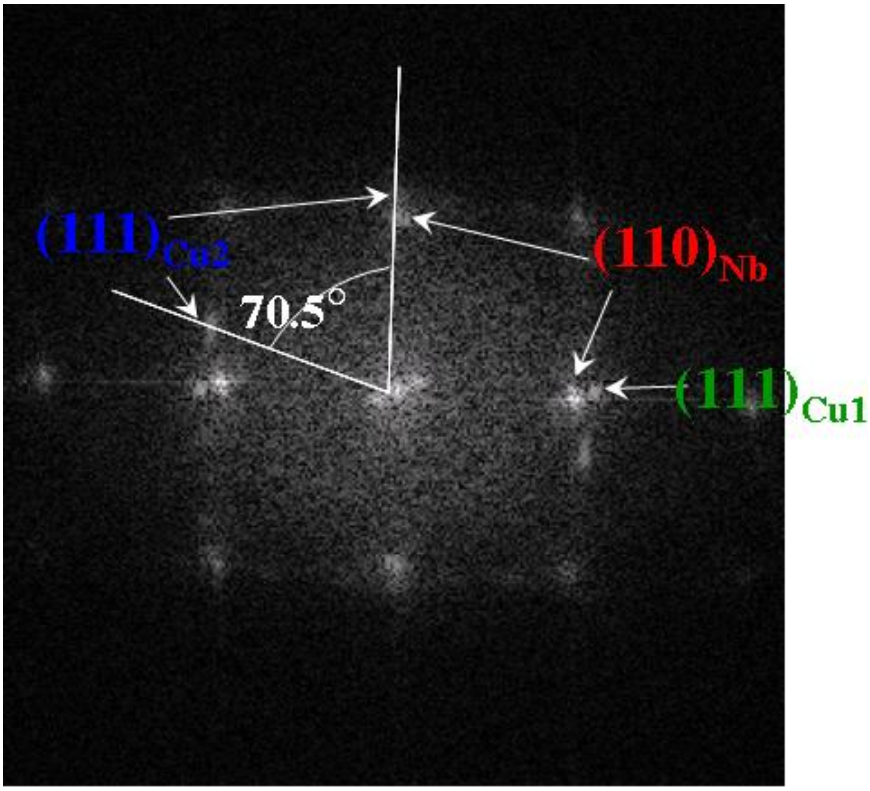


*Fig. 4.30: FFT showing diffraction from* bcc *matrix and both primary* fcc *precipitates (*fcc*1) and secondary* fcc *precipitates (*fcc*2).*

# CHAPTER 5

## CONCLUSIONS

A detailed study on the amorphization and devitrification of the immiscible Cu-Nb alloy thin films has been done. Thin films of composition Cu-45at.%Nb were prepared using the dc magnetron sputtering system. Heat-treatments of the thin films were performed inside the sputtering chamber under vacuum. Characterizations of the amorphous and heat-treated thin film samples were done using x-ray diffraction, transmission electron microscope and 3-dimensional atom probe.

1. X-ray diffraction and TEM results show that Cu-45%Nb alloy thin films are amorphous in the as-deposited condition although, 3DAP show direct evidence for nanoscale phase separation (or clustering) of Cu and Nb atoms.
2. Therefore, in case of the Cu-Nb system, the stabilization of the amorphous phase can be attributed to the nanoscale phase separation occurring in this phase.
3. At lower temperatures (200°C) the amorphous Cu-45%Nb starts crystallizing and forms nanocrystalline fcc Cu. The matrix is amorphous enriched with Nb.
4. At higher temperature (350°C), the remaining amorphous phase polymorphously crystallizes to *bcc* Nb, which is still supersaturated with Cu.
5. Annealing at a higher temperature for a longer time (390°C) it is possible that the transformation has reached completion with the remaining Cu being completely rejected.

6. The nanoscale phase separation in the amorphous phase plays a critical role in the crystallization of the Cu-45%Nb alloy thin film. They act as quenched in nuclei for the formation of nanocrystalline *fcc* Cu during the heat-treatment at 200°C.

REFERENCES

[1] S.J. Wang et al., Thin Solid Films, 2001, 394, 180.

[2] K.M. Chang et al., J. Appl Physics, 1997, 82, 1469.

[3] C.K. Hu et al., Mater. Chem Phys, 1998, 52, 5.

[4] W. Clement, R.H. Willens, P. Duwez., Nature 187 (1960) 869.

[5] P.Duwez, S.C.H Lin., J. Appl. Physics, 38 (1967) 4096.

[6] S. Kavesh in: J.J. Gilman, H.L. Leamy (Eds), Metallic Glasses, ASM International, Metals Park, OH, 1978 (Chapter 2)

[7] Turnbull D, Trans. AIME 221 (1961) 422.

[8] H.S. Chen et al., J. Chem. Phys. 48 (1968) 2560.

[9] H.S. Chen., Materials Science and Engineering, 23 (1976) 151-154.

[10] A. Peker and W.L. Johnson, App. Phys. Lett. 63 (1993) 2342.

[11] W.H. Wang, C. Dong, C.H. Shek, Mat. Sci. & Engg. R 44 (2004) 45-89.

[12] D. Turnbull, Contemp. Phys. 10 (1969) 473.

[13] D. Turnbull, Solid State Physics 3 (1956) 226.

[14] A. Angell, Science 267 (1995) 1924.

[15] W.L. Johnson, MRS Bull. 24 (1999) 42.

[16] T. Egami and Y. Waseda, J. Non-Cryst. Solids 64 (1984) 113.

[17] A. Inoue, Mater. Trans. JIM 36 (1995) 866.

[18] T. Iida, R.I.L. Guthrie, The Physical Properties of Liquid Metals Clarendon, Oxford, 1988.

[19] W. Kauzmann, Chem. Rev. 43 (1948) 219.

[20] H.J Fecht, W.L. Johnson, Nature 334 (1988) 50.

[21] R. Busch, W. Liu, W.L. Johnson, J. Appl. Phys. 83 (1998) 4134.

[22] L.E. Tanner, Acta Metall. 27 (1979) 1727.

[23] X.H. Lin, W.L Johnson, J. Appl. Phys. 78 (1995) 6514.

[24] Z.P. Lu and C.T. Liu, Acta Mater. 50 (2002) 3501-3512.

[25] A. Peker, Ph.D. Dissertation, California Institute of Technology, 1994.

[26] R. Busch, JOM 52 (7) (2000) 39.

[27] J. Eckert, JOM 52 (7) (2000) 43.

[28] E. Bakke, R. Busch, W.L. Johnson Appl. Phys. Lett. 67 (1995) 3260.

[29] A. Meyer, Phys. Rev. Lett. 80 (1998) 4454.

[30] A. Meyer, R. Busch, H. Schober, Phys. Rev. Lett. 85 (1999) 5027.

[31] U. Geyer, S. Schneider, W.L. Johnson, Y. Qiu, T.A. Tombrello, M.P. Macht, Phy. Rev.

[32] A. Masuhr et al., Time scales for viscous flow, atomic transport and crystallization in the liquid and supercooled liquid states of $Zr_{41.2}Ti_{13.8}Cu_{12.5}Ni_{10}Be_{22.5}$, Phy. Rev. Lett. 82 (1999) 2290-2293.

[33] Massalski TB, editor, Binary phase diagrams, vol 1-3, Materials Park, OH, ASM, 1986.

[34] Chien C.L. et al., Phys Rev B, 1986, 33, 3247.

[35] Childress J.R. et al., Phys Rev B, 1991, 43, 8089.

[36] Krack B.D. et al., Phys. Rev Letter, 2002, 81, 186101.

[37] Enrique R.A., J Appl Phys, 2003, 93, 2917-23.

[38] Michaelsen C, Phil Mag, 1995, A72, 813.

[39] Chen L.C et al., Nature, 1988, 336, 366.

[40] Yoshizawa et al., J. Appl. Phys, 1988, 64, 6044.

[41] Yoshizawa et al., Mater. Trans. JIM, 1991, 31, 307.

[42] Hono et al., Acta Metall Mater., 1992, 40, 2137.

[43] Hono et al., Appl. Surf. Sci., 1993, 67, 398.

[44] Hono et al., Acta Mater., 1999, 47, 997.

[45] Sakurai et al., Mater. Sci. Eng., 1994, A179, 469.

[46] Ayers et al., Acta Mater., 1998, 46, 1861.

[47] Oh et al., Scripta Mater., 2005, 53, 165.

[48] Y Zhang et al., Acta Mater., 1996, 95, 1497.

[49] T Ohkubo et al., Scripta Mater., 2001, 44, 971.

[50] E. Ma, Prog Mater. Sci, 2005, 50, 413-509.

[51] Michaelsen et al., J Appl. Phys., 1997, 81, 6024-6030.

[52] Michaelsen et al., J Appl. Phys., 1997, 81, 6024-6030.

[53] J.H. He et al., Phys. Rev Lett., 2001, 86(13), 2826-2829.

[54] J.H. He et al., Appl. Phys, Lett., 2001, 78(10), 1343-1345

[55] Hono K., Prog Mater. Sci., 2002, 47, 621.

[56] Muller EW et al., Rev Scient Instrum 1968, 39, 83

[57] Miller MK and Smith GDW, Atom probe microanalysis: principles and applications to materials problems: Pittsbutgh: Materials Research Society, 1989

[58] Tsong TT, Atom-probe field ion microscopy. Cambridge: Cambridge University Press, 1990

[59] Miller MK, Atom probe tomography: analysis at the atomic level, Kluwer, 2000

[60] Hono K, Prog. Matls. Science, 2007, 47, 621-729

[61] Muller EW et al., Rev Sci Instrument, 1968,39, 83

[62] Draschel W et al., J de Phys, 1989, 50, C8-541

[63] Waugh AR et al., Surf Sci, 1976, 61, 109

[64] Cerezo et al., Rev Sci Instrum, 1988, 59, 862

[65] Blavette et al., Rev Sci Instrum, 1993, 64, 2911

[66] Cerezo et al, App Surf Sci, 1994, 76/77, 374

[67] Deconihout et al., Ultramicroscopy, 1998, 73, 253

[68] J. C. Oh et all., *Scripta Mater*., **53**, 165 (2005).

[69] L. Kaufman and H. Nesor, *CALPHAD*, **2**(1), 81 (1978).

[70] C. Michaelson et al., *J. Appl. Phys*., **81**(9), 6024 – 6030 (1997).

[71] H. W. Sheng, W. K. Luo, F. M. Alamgir, J. M. Bai, and, E. Ma, *Nature*, **439** (7075), 419 (2006).

[72] J. H. He et al., *Phys. Rev. Lett.*, **86**(13), 2826 – 2829 (2001).

[73] J. H. He et al., *Appl. Phys. Lett.*, **78**(10), 1343 – 1345 (2001).

[74] Nastasi et al., J. Appl Phys, 1985, 58(15), 3052-3058.

[75] Kulik T., J. Non-Cryst Sol, 2001, 287, 145.

[76] Hono et al., Acta Mater., 199, 47, 997.

[77] Fan C, Inoue A, A. Mater. Trans JIM, 1997, 38, 1040.

[78] Fan et al., Apply Phys Lett, 2002, 79, 1792.